THE '4D-EARTH-SWARM' PROJECT:
RAPID GEOMAGNETIC FIELD CHANGES FROM SWARM

SCIENTIFIC REPORT
DRAFT VERSION #3

a project supported by ESA

March 2021

list of partners:

- ISTerre, Grenoble, France (PI)
- ETH Zurich, Switzerland
- Univ. of Leeds, UK
- IPG Paris, France
- DTU Space, Copenhagen, Denmark

Contents

Chapter 1

Review of the state of the art in interannual core dynamics

4DEarth_Swarm_Core ESA project deliverable R-A.1

A. Jackson[1], N. Gillet[2], J. Aubert[3], C. Finlay[4], D. Jault[2], P. Livermore[5] and J. Noir[1], N. Olsen[4]
[1] ETH Zurich, [2] ISTerre, [3] IPG Paris, [4] DTU Space, [5] University of Leeds

1.1 Context of the 4D-Earth-Swarm activities

Our activities are broadly characterised by one scientific question, namely the physical modeling of rapid secular variation (SV, or rate of change of the magnetic field) changes. These are inter-annual changes with time scales of two years to several decades. The question will be tackled using several angles of investigation, including:

- the modeling of geomagnetic data by means of reduced stochastic models of the core surface dynamics, based on satellite observations through (stochastic) data assimilation algorithms;
- the physical modeling of such SV changes through reduced quasi-geostrophic (QG) models that describe the dynamics of axially invariant motions in the core in the presence of magnetic field;
- the comparison of SV changes observed through satellite (Swarm and others) data with outputs from three-dimensional computations.

These are further described in the sections below.

1.2 Background

Swarm data hold the prospect of illuminating interior properties of the core, such as the strength and distribution of magnetic fields and, potentially, the strength of buoyancy forces. The observed spatio-temporal changes can be related to a model of the electrically conducting core's interior dynamics, provided that a predictive dynamical model of those dynamics is available. However, only in very special

circumstances is such a deterministic model already available. It is the case for torsional oscillations (namely the oscillations of cylinders of fluid coaxial with the rotation axis, where the restoring force is entirely magnetic), used by Gillet et al (2010) to determine one property of the interior magnetic field from inter-annual changes in the fluid flow over the last few decades. In no other case is a dynamical model available for the study of the rapid (i.e. decadal and shorter) geomagnetic field changes. The exploration of suitable strategies for the creation of a model applicable to Swarm data is one of the aims of the present proposal. The accepted state of the art for combining observations with a dynamical model is termed data assimilation (DA). At present there are two flavours of DA which are available to the geomagnetic community: probabilistic (here sequential) assimilation (SDA) and variational assimilation (VDA). The sequential approach in the context of primitive magneto-hydro-dynamic equations has been pioneered by A. Fournier & J. Aubert and colleagues at IPGP and W. Kuang & A. Tangborn at NASA. More and more groups are adopting this approach, including groups in Germany and Japan.

Recently, SDA was also considered to tackle questions posed by satellite observations by means of two pragmatic approaches: either through no-cast re-analyses (i.e. no time-stepping of the deterministic model) using three-dimensional geodynamo model cross-covariances (Aubert, 2015), or by considering instead a stochastic forecast model anchored to geodynamo spatial covariances and compatible with the occurrence of geomagnetic jerks (Barrois et al, 2017).

The variational approach has been applied to simplified problems by Li et al (2014). In principle, the mechanics of this approach are in hand, but there is a need to develop a suitable model to which this approach could be applied that does not suffer from the effects of overly-large viscosity. The idea for a variational approach was also set out in Canet et al (2009) and applied to the problem of torsional oscillations.

A number of potential avenues are open for the development of a new dynamical model. We believe that there are close parallels with similar problems in oceanography, whose community has worked for many years to develop models in which the effect of viscosity is not overbearing.

We mention promising avenues: Canet et al (2009) and Labbé et al (2015) have developed a QG model of core dynamics that holds the promise of development into a suitable dynamical model for assimilation. While most of the terms in the Navier-Stokes equation can be elegantly handled by these approaches, neither of the models are able to properly treat the magnetic terms in a rigorous manner. This family of approaches will be stepping-off points in our quest to develop a suitable dynamical core for assimilation.

In the following sections we discuss the pertinent observations and techniques that have been developed by the community, what they tell us, and what is the state of play.

1.3 Origin and observability of interannual motions observed

A consensus view of the 4D Earth team is that it is a regrettable situation that the 6 year torsional oscillations have only been observed by one team, namely the original discoverers (Gillet et al, 2010). Despite the strong evidence from the predicted length-of-day (LOD) changes that correspond well to the observed changes (Gillet et al, 2015), there is a need for an independent corroboration of these motions (even though the above observation has been confirmed with several rather distinct algorithms, see Gillet et al, 2019). This was never proposed as part of the WPs of the present proposal, but, considering the importance of the observation for core dynamics, it is to be hoped that a scientific team will take up the challenge. A key ingredient in the isolation of torsional oscillations at interannual periods by the Grenoble group is the inclusion of unmodelled SV sources associated with time-correlated subgrid processes. We believe any attempt at reproducing this result should involve this mechanism, in order to avoid either losing information by under-fitting SV data, or generating severely biased core flow models by over-fitting them.

The strongest repeating signal in LOD series is at 6 years (Abarca Del Rio et al, 2000; Chao et al, 2014; Holme and De Viron, 2013). Filtered around this period, core flow models inverted from SV models show an outward propagation of zonal motions. When interpreted as torsional Alfvén waves (Braginsky, 1970), the recovered wave form raises several geophysical issues. First the absence of noticeable reflexion at the equator may be interpreted in term of a relatively weak conductance of the lower mantle (of the order of $3\,10^7$ S), in a scenario where the core-mantle coupling is operated through an electro-magnetic stress (Schaeffer and Jault, 2016). However, there is still the possibility for a topographic torque to be responsible for the associated LOD changes (see §1.9).

Second, the propagation from the inner core (at least during the 1960-70's) has been first interpreted through a torque involving the inner core. This latter may be associated with Lorentz forces on the vicinity of the tangent cylinder (Teed et al, 2015), as it is the case in dynamo simulations (Schaeffer et al, 2017). Alternatively, it may involve a gravitational coupling between the inner core and the mantle (Mound and Buffett, 2006), although this scenario itself is debated (Davies et al, 2014; Chao, 2017). The possibility of an excitation induced by magnetospheric field changes has been proposed (Legaut, 2005), but there may not be enough energy there to excite torsional Alfvén waves (by definition equi-partitioned in kinetic and magnetic energies) with the observed amplitude. Finally, one cannot rule out the possibility of a forcing spread throughout the fluid core, as we have only access to the gravest of the torsional modes (Gillet et al, 2017). The question whether the better spatio-temporal resolution offered by Swarm data will give or not access to higher harmonics is open.

Regardless, one should keep in mind that the above zonal flows only represent

a tiny contribution to interannual motions (Gillet et al, 2015; Kloss and Finlay, 2019), and that we still miss a conclusive interpretation of the more energetic non-zonal motions (see also §1.6). We also stress the limited access to interannual field changes, which are constrained by observations only for the largest length-scales in geomagnetic field models (Gillet, 2019).

1.4 Basic mechanisms for core-mantle coupling, and settled questions

Core-mantle coupling plays an important part in the time evolution of the LOD, with periods above 2 years, and in the dissipation of the annual retrograde nutation of the Earth's rotation axis. Changes of axial core angular momentum are estimated from models of the geostrophic motions in the Earth's fluid core and changes of axial mantle angular momentum are directly inferred from LOD observations. There is reasonable evidence that variations in the core and mantle axial angular momentum compensate although uncertainties remain significant (Gillet et al, 2015; Bärenzung et al, 2018). Curiously, the agreement appears less good during the satellite era, from $\approx$ 2003 onward (Gillet et al, 2019). The core-mantle coupling mechanism responsible for the exchanges of angular momentum between the fluid core and the solid mantle is still debated.

The most widely studied coupling mechanisms between core and mantle are viscous, gravitational, topographic and electromagnetic (EM). Unfortunately they all depend on poorly known properties of the lowermost mantle and core, respectively the effective core viscosity, geometry of the gravity equipotential surface next to the core-mantle boundary, topography of the core-mantle interface and the electrical conductivity of the lowermost mantle (Roberts and Aurnou, 2011). Of these, we briefly review EM coupling below as this is most relevant to the 4D-Earth-Swarm proposal.

Studies of EM sounding from Earth's surface based on external magnetic field fluctuations have poor sensitivity to the lowermost mantle, although typical values are 10 S/m (Constable, 2007). Yet due to inhomogeneities on the core-mantle boundary, these values may not be indicative of the conductivity at the interface itself. The difficulty in determining conductivity is further compounded by the fact that EM coupling mechanisms generally depend on conductance, the integrated conductivity over a layer (whose thickness is unknown), rather than the conductivity itself.

Independently, through respectively models of EM coupling and consideration of nutations, both Holme (1998) and Buffett et al (2002) propose a conductance of 10^8 S. One possibility is this is caused by a thin layer (of about 200 m) of material with the same conductivity of the core. The occurrence of a solid metallic layer at the lowermost mantle pressure and temperature is problematic and the mechanism of nutation dissipation remains an open question (Buffett, 2010). Even if the conducting materials are distributed over a thicker region, it is difficult to avoid a layer

of relatively conductive material on the core-mantle boundary (CMB) interface as on treating the majority of the lowermost mantle as a single layer of depth 1000 km would yield a conductance of 10^7 S, inconsistent with other estimates. However, this reasoning does not hold if other mechanisms participate in the coupling of the core with the mantle as the required EM torque would be lower.

Another line of investigation comes from jointly considering dynamics in the core interior and interactions with the mantle. For example, torsional waves, which propagate as Alfv́en waves in the Earth's core, have periods about 6 years. Their reflection upon arrival at the core equator depends on the electrical conductance of the lowermost mantle (Schaeffer and Jault, 2016). They are completely absorbed for a mantle conductance of $1.6 \pm 0.3 \times 10^8$ S (error bar arising from uncertainties on the intensity of the radial magnetic field at the core equator). The apparently weak reflection of the waves leads to estimates of total mantle conductance in the range $3 \times 10^7 - -3 \times 10^8$S. All the above estimates offer consistent values of the conductance of about 10^8 S, although the actual electrical conductivity at the CMB is not well constrained.

Most dynamo simulations do not include magnetic core-mantle coupling. The recent geodynamo study of Aubert and Finlay (2019) dedicated to the rapid dynamics of the Earth's core however does include a thin mantle layer of conductance of about 2×10^8 S, *i.e.* comparable to the above values.

1.5 How good is the quasi-geostrophic assumption?

In rotating fluid dynamics, a geostrophic equilibrium is a balance between Coriolis and pressure forces. The only truly geostrophic motions in a rotating spherical shell are zonal (axisymmetric azimuthal) flows with axial invariance. All other flows (including convective poloidal motions) rather obey a degenerate form of geostrophy which is known as quasi-geostrophy (QG) at the condition that the first-order forces driving those flows are much weaker than the leading-order pressure and Coriolis forces. Because of the Taylor-Proudman theorem, QG flows generally acquire a quasi-invariant structure along the rotation axis when the first-order forces are sufficiently weak, leading to the possibility to formulate their dynamics in framework of reduced dimensionality (e.g. Gillet and Jones, 2006; Labbé et al, 2015; Calkins, 2018). This in turn enables important computer cost savings when performing numerical simulations, and the possibility to reach strongly turbulent regime that are appropriate for planetary cores (e.g. Gastine, 2019). QG has proven to be an efficient way to describe rapidly-rotating thermal convection (e.g. Gillet and Jones, 2006). In this non-magnetic case, the results compare favourably with three-dimensional reference models and laboratory experiments, particularly concerning the scaling behaviour in turbulent conditions (Aubert et al, 2003; Gastine et al, 2016; Guervilly et al, 2019) because the first-order buoyancy and inertial forces remain sufficiently subdominant relative to the leading-order QG equilibrium.

Systematic surveys of three-dimensional numerical dynamos (Schwaiger et al, 2019) performed over a wide range of the accessible parameter space (including conditions approaching those of the Earth's core, Aubert et al, 2017) have confirmed the existence of a leading-order QG equilibrium even in the presence of a self-sustained magnetic field. Magnetostrophy, where the magnetic force can reach leading order and balance the Coriolis and pressure forces, is never observed at system scale (because the system needs buoyant driving) and is usually deferred to scales of about 100 km, but can approach larger scales in selected regions of the parameter space where the convective forcing is low (Dormy, 2016; Schwaiger et al, 2019). In all simulations, the occurrence of local magnetostrophy corresponds to the Lorentz force being reduced to a magnetic pressure gradient without a dynamical influence, meaning that from a dynamical standpoint QG in fact holds at all scales. In the numerical dynamos, the first-order force balance coming after QG is between the Lorentz, buoyancy forces and the ageostrophic part of the Coriolis force. This balance is known as the MAC balance and the total (leading plus first) order force balance is referred to as the QG-MAC balance. The first-order MAC balance is additionally scale-dependent. At scales larger than about 1000 km the first-order balance is mainly of thermal wind nature (balance between the ageostrophic Coriolis and buoyancy forces), with the magnetic force being subdominant. The scale-dependence of the force balance can also be viewed as a frequency-domain dependence, where time scales longer than the secular overturn are mainly governed by thermal wind dynamics and the role of magnetic forces is deferred to faster, interannual to decadal dynamics (Schaeffer et al, 2017; Aubert, 2018). This corresponds to a minimisation of the interaction between the magnetic field and the flow if sufficient time is allowed for the moderating effects of Lenz' law to take place.

Unlike non-magnetic rotating convective systems, numerical dynamos frequently feature a first-order MAC balance less than an order of magnitude below the leading-order QG equilibrium (Schwaiger et al, 2019). Because of this, the slowly-varying (secular) flows can show departures from QG and axial invariance, and need to be removed in order to exhibit structures closer to QG that can be modelled as such in two space dimensions. Of particular importance are magneto-inertial waves such as interannual Alfvén waves, which have been observed in numerical simulations at the axisymmetric (e.g. Schaeffer et al, 2017) and non-axisymmetric (Aubert, 2018) levels. These latter QG, axially invariant, non-axisymmetric waves have been related to the occurrence of geomagnetic jerks (Aubert and Finlay, 2019), underlining the relevance of a QG framework to describe the geomagnetic signal at interannual time scales. The main difficulty is that the waves ride on a three-dimensional, strongly heterogeneous, slowly evolving thermal and magnetic background state that cannot readily be described within a QG framework, as stated above. This rationalises the general difficulty encountered by the community in obtaining working self-sustained dynamos that are purely QG, while more success has been obtained by studies where QG flows are produced within an imposed, rather than self-sustained, magnetic field (e.g. Labbé

et al, 2015; More and Dumberry, 2017)

In summary, QG is a numerically efficient and easy to implement approximation, that has potential to describe some of the interannual core dynamics. The insight from current three-dimensional numerical dynamos however suggests that in the presence of a self-sustained magnetic field, a QG description of core dynamics most likely fails to describe the slowly-varying, buoyancy-driven secular evolution of the core that generates the field. The way to progress may therefore consist in an estimation of a three-dimensional background state (thermal, magnetic, kinematic) for the core at present (during the Swarm era), over which a QG model may be built to describe the rapidly-evolving part of the geomagnetic signal as an induced perturbation of an imposed background field.

1.6 Stochastic models anchored to geodynamo spatial covariances

There is currently a debate concerning the existence of a specific signal at 6 yr in the magnetic field. On the one hand, secular acceleration (SA) pulses, or maxima in the SA norm, seem to occur every 3 yrs (e.g. Finlay et al, 2016). This may either result from a SV signal specific to the 6 yr period (e.g. Soloviev et al, 2017), or be the consequence of the filtering in space and time when building global models (Gillet, 2019). The existence of jerks events isolated in time is particularly intriguing since we are aware of no other geophysical system displaying such a behavior. Alternatively, SA pulses could result from the spectral index $\alpha \simeq -2$ found for the temporal spectrum of SV Gauss coefficients at decadal to annual time-scales, $S(f) \propto f^{\alpha}$ (Lesur et al, 2017).

In this context, one expects the SA temporal spectrum to be flat from annual to decadal periods. The framework of stochastic processes has thus been considered for the integration of magnetic field evolution into SDA tools that only model the core surface dynamics, still incorporating geodynamo constraints by means of spatial and temporal cross-covariances (Barrois et al, 2017; Gillet et al, 2019). This approach presents the advantage of reducing considerably the dimension of the model state w.r.t. geodynamo driven DA algorithms (e.g. Fournier et al, 2013; Sanchez et al, 2019). It also extends down to annual periods the range of frequencies where the -2 spectral index operates (extreme 3D simulations, once scaled to geophysical units, lose this property at about 30 yr periods (Aubert, 2018), i.e. outside the very period range of interest for this proposal). The main current limitation of stochastic models is their inability to directly relate the observed SV changes to dynamical properties deep in the fluid core (though its products can be used as a constraint for subsequent dynamical analysis).

1.7 The role of buoyancy and of Lorentz forces

In geodynamo simulations run at high rotation rates (Schaeffer et al, 2017; Aubert et al, 2017), Lorentz forces appear to play a relatively minor role at large length-scales, and this despite a large magnetic field intensity (as measured by Elsasser numbers of order unity). Magnetic and velocity fields seem to self-organize so as to minimize induction as much as possible. The magnetostrophic equilibrium (where both Lorentz and Coriolis forces balance the pressure gradient) is thus expelled towards small length-scales (Aurnou and King, 2017), while geostrophy applies at the largest length-scale, at which departures from geostrophy are buoyancy-driven. If this scenario applies in the Earth's core, models based on magnetostrophy (see Hardy et al, 2018) might miss a crucial ingredient in order to model decadal field changes – one may think here in particular of QG models based on quadratic quantities of the magnetic field (see Jault and Finlay, 2015).

Numerical dynamos along the path are nevertheless run at parameters different from Earth-like, involving parameterizations of some nonlinear subgrid processes (Aubert et al, 2017). With lower values of the magnetic Prandtl number P_m (ratio of viscous to magnetic diffusivities), the larger magnetic diffusion may tend to enlarge the range of wave-numbers where magnetostrophy prevails. This issue is particularly important on the vicinity of the tangent cylinder. In this singular area of the core, simulations show intense magnetic fields in link with strong polar vortices (Schaeffer et al, 2017)

1.8 The prospects and applicability of the quasi-geostrophic hypothesis

We have seen in previous sections that the idea of quasi-geostrophy is attractive, as it captures much of the required physics. In the hydrodynamical case, where there are no magnetic forces, the approach can be readily used to model buoyancy-driven flows, to great effect (Guervilly et al, 2019). Presently what is missing is a theory that is able to handle the Lorentz forces that arise in the presence of magnetic fields.

A first attempt at the problem was made by Canet et al (2009). The approach to project the dynamical equations onto the equatorial plane involves an integration along the rotation axis from the lower to the upper boundary. This integration leads to boundary terms that are, unlike all other quantities, controlled by values of electrical currents that are not describable on the equatorial plane. It was initially envisaged that these boundary terms would be much smaller than the volumetrically averaged terms and thus could be neglected (Canet et al, 2009). Subsequent work by Maffei (2016), amongst others, showed the difficulties that this leads to: when one considers the normal mode problem of small oscillations around a background state, one finds that the surface terms are non-negligible, particularly close to the equator. This leads to an incorrectly-posed eigenvalue problem.

Recognising this issue, Labbé et al (2015) pioneered a new approach. They

showed that if the magnetic field could be written in the same form as the QG velocity field, then the projection of all quantities onto the equatorial plane could be achieved. This is a great step forward. It comes at a price however. The system treated means that the field lines of the magnetic field close within the fluid, and no field emanates from the core. In some ways this is similar to the treatment of Canet et al (2009). More worrying is the likelihood that a magnetic field in the core can really be represented in this QG form. The QG form for the velocity field is well motivated, relying, as it does, on the underpinnings provided by the Proudman-Taylor theorem, which leads naturally to first-order geostrophy. There is no such theorem that suggest that the QG form can be used for the magnetic field. Thus one must wonder to what extent the results will depend on this assumption.

To summarise, there is no presently acceptable magnetohydrodynamical QG formulation, and it remains a challenge for the future to develop one. The attractiveness of the approach, if a self-consistent one can be found, lies in its use for the purposes of data assimilation.

The data assimilation problem is the following. One has high quality maps of the magnetic field at the core-mantle boundary for the last decades and centuries that have been created from measurements taken at the Earth's surface and above. These will subsequently be termed *observations*, despite the fact that the maps are actually derived quantities. The quest is to find a dynamical model of motions in the core (and their time variations) that can account for the observations. The problem requires a *dynamical core*, namely a version of the fluid mechanics in the core. With these two ingredients, the matching process can begin. The outcome of the matching process is twofold. In principle one can deduce properties of the core such as the time-dependent buoyancy field and the interior magnetic field strength and geometry. These quantities are such that they lead to a dynamical evolution in time of core quantities, such that the observations are honoured. But in addition, the time-evolution can be followed forwards beyond the time window of the observations, into a prediction. This comes naturally, for free.

The attractiveness of the QG approach as a version of the fluid mechanics is twofold. Firstly it can operate in regimes that three dimensional dynamo models cannot reach. In particular, it is able to reduce the effects of viscosity to levels that are close to those expected within the core (Guervilly et al, 2019). More important considerations, however, are probably associated with the inverse problem that is being solved. Quite likely it is only possible to recover some forms of "lumped parameters", rather than full 3-D information. Thus one may have to be satisfied with field strengths and geometries reduced by averaging, rather than full recovery of 3-D toroidal and poloidal magnetic fields. Put simply, 2-D observations in time (observations on the core-mantle boundary) are unlikely to be able to recover 3-D fields. These 2D fields may well be able to recover 2-D fields as a function of time. Thus the pure counting problem argues in favour of a theory like quasi-geostrophy. The problem was highlighted by Li et al (2014).

It should be said that there has been considerable success by using 3D dynamo models as dynamical cores for Ensemble Kalman filter schemes. However, these

calculations have not been able to constrain the interior buoyancy and magnetic fields in the core.

It is our hope that the present 4DEarth activity might lead to further insights and experiences that will lay the path for future data assimilation activities.

1.9 Topographic torques on a non-spherical core

So far there is no certainty in the mechanism that transfers core's angular momentum to the solid mantle. Proposed mechanisms include electromagnetic coupling via electrically conducting lower mantle (see section 1.4 for more details), gravitational coupling via a gravitational torque between a deformed inner core and the mantle (Buffett, 1996a,b), or topographic coupling through a non-axisymmetric CMB.

For a spherical CMB the pressure torque on the mantle by any flow in the core vanishes exactly by definition. More precisely, for any CMB symmetric about the rotation axis, no changes in the LOD may be explained by the pressure torque. Investigating core flows in non-axisymmetric domains is challenging and has been limited to a few studies up until today (e.g. Kuang and Chao, 2001; Jault and Finlay, 2015; Vidal et al, 2019).

Torsional waves, with periods on the scale of a few years, have been proposed to be responsible for such changes in the LOD. Their periods have been used to infer the mean radial magnetic field strength in the core, a quantity otherwise inaccessible to observations (Gillet et al, 2010). In a sphere, the flow of these waves follow contours of constant column height. To investigate the flow structure of these waves for a non-axisymmetric domain and wether or not this flow is capable of exerting a pressure torque onto the solid boundary is the goal of this task. We aim to use a Cartesian monomial approach in the ellipsoid (Vidal et al, 2019) and curvilinear coordinates for any geometry beyond the ellipsoid.

It is unknown how important domains without closed geostrophic contours are for the topographic torque. Such domains are certainly present in the Earth's core. Understanding the influence of topography on the flow structure and periods of torsional waves is crucial to verify their robustness in predicting core quantities in any planetary or stellar core.

1.10 Conclusions

There have been spectacular achievements in core studies over the last decade. Not least is the observation of torsional oscillations. We have alluded to some of the open issues in preceding sections. Although much is understood, it has proven difficult to deduce concrete properties of the Earth. Tables 1 and 2 summarise the state of play on the most important issues.

State of the art on lower mantle electrical conductivity σ
From observed lack of reflected torsional oscillations: Only bounds are on conductance $G = \sigma H$, where H is the depth of the conducting region. Constraint is on $Q = \sqrt{\frac{\mu_0}{\rho}} G B_r\|_{z=0} \approx 10^{-5} G B_r\|_{z=0}$ (SI) where $G = \int_{r_0}^{r_0+H} \sigma \, dr \approx \sigma H$. $Q \simeq 1$ is preferred.
Pros: This is the strongest constraint on conductance.
Cons: Need definitive bounds on reflection coefficient/reflected energy. Need bounds on radial field B_r at $z = 0$. Provides information on only one region of CMB, at the equator. Most of CMB entirely unconstrained. Conductance not required to be laterally homogeneous, could have isolated blobs. Theory for laterally heterogeneous conductance yet to be worked out.

Table 1.1: State of the art on lower mantle electrical conductivity σ at the base of the mantle.

State of the art on interior field strength
Gillet et al (2010,2015) provide a lower bound of 2-3mT in the cylindrically radial magnetic field strength. The profile of B_s shows weakening towards the CMB.
Pros: Almost exactly predicts the filtered length-of-day in the 5-8 year period range.
Cons: Has never been replicated.

Table 1.2: State of the art on interior field strength in the Earth's core.

Bibliography

Abarca Del Rio R, Gambis D, Salstein D (2000) Interannual signals in length of day and atmospheric angular momentum. In: Annales Geophysicae, Springer, vol 18(3), pp 347–364

Aubert J (2015) Geomagnetic forecasts driven by thermal wind dynamics in the Earth's core. Geophys J Int 203(3):1738–1751

Aubert J (2018) Geomagnetic acceleration and rapid hydromagnetic wave dynamics in advanced numerical simulations of the geodynamo. Geophys J Int 214(1):531–547

Aubert J, Finlay CC (2019) Geomagnetic jerks and rapid hydromagnetic waves focusing at Earth's core surface. Nature Geosci 12(5):393–398, DOI 10.1038/s41561-019-0355-1

Aubert J, Gillet N, Cardin P (2003) Quasigeostrophic models of convection in rotating spherical shells. Geophys Geochem Geosystems 4

Aubert J, Gastine T, Fournier A (2017) Spherical convective dynamos in the rapidly rotating asymptotic regime. J Fluid Mech 813:558–593

Aurnou J, King E (2017) The cross-over to magnetostrophic convection in planetary dynamo systems. Proceedings of the Royal Society A: Mathematical, Physical and Engineering Sciences 473(2199):20160,731

Bärenzung J, Holschneider M, Wicht J, Sanchez S, Lesur V (2018) Modeling and predicting the short-term evolution of the geomagnetic field. Journal of Geophysical Research: Solid Earth 123(6):4539–4560

Barrois O, Gillet N, Aubert J (2017) Contributions to the geomagnetic secular variation from a reanalysis of core surface dynamics. Geophys J Int 211(1):50–68

Braginsky S (1970) Torsional magnetohydrodynamics vibrations in the earth's core and variations in day length. Geomagn Aeron 10:3–12

Buffett BA (1996a) Gravitational oscillations in the length of day. Geophysical Research Letters 23(17):2279–2282, DOI 10.1029/96GL02083

Buffett BA (1996b) A mechanism for decade fluctuations in the length of day. Geophysical Research Letters 23(25):3803–3806, DOI 10.1029/96GL03571

Buffett BA (2010) Chemical stratification at the top of earth's core: Constraints from observations of nutations. Earth and Planetary Science Letters 296(3-4):367–372

Buffett BA, Mathews PA, Herring TA (2002) Modelling of nutation and precession: Effects of electromagnetic coupling. J Geophys Res 107(B4):5.1–5.15

Calkins MA (2018) Quasi-geostrophic dynamo theory. Phys Earth Planet Int 276:182 – 189

Canet E, Fournier A, Jault D (2009) Forward and adjoint quasi-geostrophic models of the geomagnetic secular variation. J Geophys Res: Solid Earth 114(B11)

Chao B (2017) Dynamics of axial torsional libration under the mantle-inner core gravitational interaction. Journal of Geophysical Research: Solid Earth 122(1):560–571

Chao BF, Chung W, Shih Z, Hsieh Y (2014) Earth's rotation variations: a wavelet analysis. Terra Nova 26(4):260–264

Constable S (2007) Geomagnetism. Treatise on Geophysics, ed Schubert, G, Elsevier

Davies CJ, Stegman DR, Dumberry M (2014) The strength of gravitational core-mantle coupling. Geophysical Research Letters 41(11):3786–3792

Dormy E (2016) Strong-field spherical dynamos. J Fluid Mech 789:500–513

Finlay CC, Olsen N, Kotsiaros S, Gillet N, Tøffner-Clausen L (2016) Recent geomagnetic secular variation from Swarm. Earth, Planets and Space 68(1):1–18

Fournier A, Nerger L, Aubert J (2013) An ensemble Kalman filter for the time-dependent analysis of the geomagnetic field. Geochem geophys geosyst 14(10):4035–4043

Gastine T (2019) pizza: an open-source pseudo-spectral code for spherical quasi-geostrophic convection. Geophysical Journal International 217(3):1558–1576, DOI 10.1093/gji/ggz103, URL https://doi.org/10.1093/gji/ggz103, http://oup.prod.sis.lan/gji/article-pdf/217/3/1558/28225303/ggz103.pdf

Gastine T, Wicht J, Aubert J (2016) Scaling regimes in spherical shell rotating convection. Journal of Fluid Mechanics 808:690–732, DOI 10.1017/jfm.2016.659

Gillet N (2019) Spatial And Temporal Changes Of The Geomagnetic Field: Insights From Forward And Inverse Core Field Models. In: Geomagnetism, aeronomy and space weather: a journey from the Earth's core to the sun, URL https://hal.archives-ouvertes.fr/hal-02042703

Gillet N, Jones CA (2006) The quasi-geostrophic model for rapidly rotating spherical convection outside the tangent cylinder. J Fluid Mech 554:343–369

Gillet N, Jault D, Canet E, Fournier A (2010) Fast torsional waves and strong magnetic field within the Earth's core. Nature 465(7294):74

Gillet N, Jault D, Finlay C (2015) Planetary gyre, time-dependent eddies, torsional waves, and equatorial jets at the earth's core surface. Journal of Geophysical Research: Solid Earth 120(6):3991–4013

Gillet N, Jault D, Canet E (2017) Excitation of travelling torsional normal modes in an earth's core model. Geophysical Journal International 210(3):1503–1516

Gillet N, Huder L, Aubert J (2019) A reduced stochastic model of core surface dynamics based on geodynamo simulations. Geophys J Int 219(1):522–539

Guervilly C, Cardin P, Schaeffer N (2019) Turbulent convective length scale in planetary cores. Nature 570(7761):368–371

Hardy CM, Livermore PW, Niesen J, Luo J, Li K (2018) Determination of the instantaneous geostrophic flow within the three-dimensional magnetostrophic regime. Proceedings of the Royal Society A: Mathematical, Physical and Engineering Sciences 474(2218):20180,412

Holme R (1998) Electromagnetic core-mantle coupling ii: probing deep mantle conductance. The core-mantle boundary region 28:139–151

Holme R, De Viron O (2013) Characterization and implications of intradecadal variations in length of day. Nature 499(7457):202

Jault D, Finlay CC (2015) Waves in the core and mechanical core-mantle interactions. In: Schubert G, Olson P (eds) Treatise on Geophysics, Core Dynamics, 2nd edition, vol 8, Elsevier, Oxford, chap 8.09, pp 225–244

Kloss C, Finlay CC (2019) Time-dependent low-latitude core flow and geomagnetic field acceleration pulses. Geophysical Journal International 217(1):140–168

Kuang W, Chao BF (2001) Topographic core-mantle coupling in geodynamo modeling. Geophysical research letters 28(9):1871–1874

Labbé F, Jault D, Gillet N (2015) On magnetostrophic inertia-less waves in quasi-geostrophic models of planetary cores. Geophys Astrophys Fluid Dyn 109(6):587–610

Legaut G (2005) Ondes de torsion dans le noyau terrestre. PhD thesis, Univ. Joseph Fourier

Lesur V, Wardinski I, Baerenzung J, Holschneider M (2017) On the frequency spectra of the core magnetic field Gauss coefficients. Phys Earth Planet Int

Li K, Jackson A, Livermore PW (2014) Variational data assimilation for a forced, inertia-free magnetohydrodynamic dynamo model. Geophysical Journal International 199(3):1662–1676

Maffei S (2016) Quasi-geostrophic models for fast dynamics in the earth's outer core. PhD thesis, ETH Zurich

More C, Dumberry M (2017) Convectively driven decadal zonal accelerations in Earth's fluid core. Geophysical Journal International 213(1):434–446

Mound JE, Buffett BA (2006) Detection of a gravitational oscillation in length-of-day. Earth and Planetary Science Letters 243(3-4):383–389

Roberts PH, Aurnou J (2011) On the theory of core-mantle coupling. Geophys Astrophys Fl Dyn 106(2):157–230

Sanchez S, Wicht J, Bärenzung J, Holschneider M (2019) Sequential assimilation of geomagnetic observations: perspectives for the reconstruction and prediction of core dynamics. Geophysical Journal International 217(2):1434–1450

Schaeffer N, Jault D (2016) Electrical conductivity of the lowermost mantle explains absorption of core torsional waves at the equator. Geophysical Research Letters 43(10):4922–4928

Schaeffer N, Jault D, Nataf HC, Fournier A (2017) Turbulent geodynamo simulations: a leap towards Earth's core. Geophys J Int 211(1):1–29

Schwaiger T, Gastine T, Aubert J (2019) Force balance in numerical geodynamo simulations: a systematic study. Geophys J Int 219(S1):S101–S114

Soloviev A, Chulliat A, Bogoutdinov S (2017) Detection of secular acceleration pulses from magnetic observatory data. Physics of the Earth and Planetary Interiors 270:128–142

Teed RJ, Jones CA, Tobias SM (2015) The transition to earth-like torsional oscillations in magnetoconvection simulations. Earth and Planetary Science Letters 419:22–31

Vidal J, Cébron D, ud Doula A, Alecian E (2019) Fossil field decay due to nonlinear tides in massive binaries. Astronomy & Astrophysics 629:A142, DOI 10.1051/0004-6361/201935658

Chapter 2

Geomagnetic Datasets

4DEarth_Swarm_Core ESA project deliverable D-B.1

C. C. Finlay and M. D. Hammer
DTU Space, Technical University of Denmark

2.1 Introduction

This report provides information on geomagnetic datasets and derivatives (including geomagnetic field models) produced by DTU for the Swarm+ 4D Deep Earth: Core project, as part of Task B and Work Package 1, and designed to be used for studies on core dynamics.

2.2 Geomagnetic Virtual Observatory datasets

Geomagnetic Virtual Observatory (GVO) datasets have been produced in a consistent fashion from the satellite missions CHAMP, Cryosat-2 and *Swarm*. In each case the same algorithm, recently developed in the context of the *Swarm* mission (Hammer et al, 2020a) was been employed.

Each GVO dataset involves time series of the vector magnetic field on a regular grid at satellite altitude. They were constructed by fitting a local potential to the data falling within cylinders centered on each target location (Mandea and Olsen, 2006; Olsen and Mandea, 2007). The geographical locations of the GVOs and associated cylinders (radius 700 km) used to construct the GVO datasets delivered here are shown in Fig. 2.1. This grid was generated using a recursive zonal approximate equal area partitioning algorithm (Leopardi, 2006).

Detailed tests of the GVO algorithm have recently been carried out in the context of the *Swarm* mission (Hammer et al, 2020a,b,d). Here we go further and apply the same data selection and processing procedure to data from the earlier CHAMP mission (Reigber et al, 2005) and the Cryosat-2 mission, where calibrated platform magnetometer data has recently become available (Olsen et al, 2020). Below we give a brief summary of the GVO processing algorithm, full details are given in the *Swarm* GVO product description of algorithm document

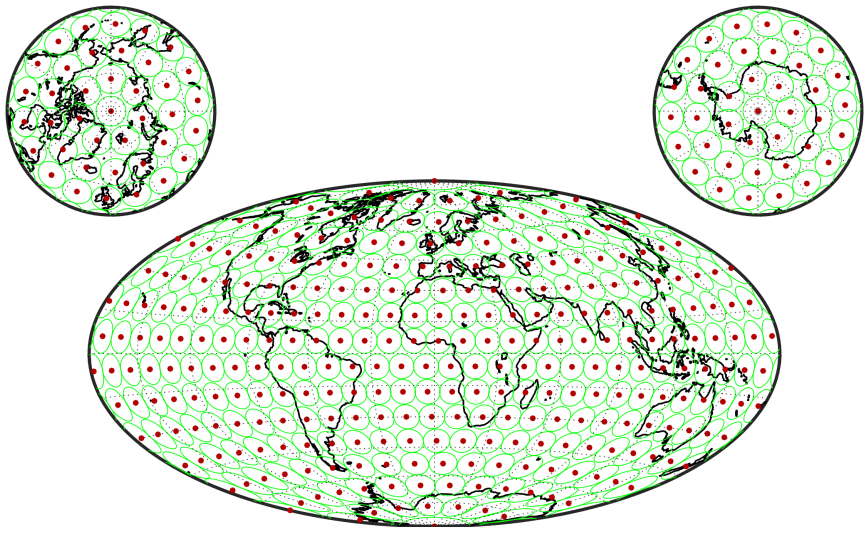

Figure 2.1: Geomagnetic Virtual Observatory (GVO) locations (red dots) along with associated regions where satellite data is collected (green circles). 300 locations in all, arranged in an approximately equal area grid.

(Hammer et al, 2020b).

GVO series are provided at 1 month and 4 month cadences. In each case estimates are provided for both the observed field (including all data sources) and the core field. 1 monthly GVOs are derived from 15 sec samples of *Swarm* L1b MAG-L data, from all three satellites, and 15 sec samples of L3 CHAMP data. 4 monthly GVOs are derived from 15 sec samples of *Swarm* L1b MAG-L data, 15 sec samples of L3 CHAMP data, and 1 minute means of Cryosat-2 data, that satisfy the following dark and geomagnetically quiet time criteria:

- The sun is at least 10° below horizon
- Geomagnetic activity index $K_p < 3°$
- Time change of Ring current (RC) index $|dRC/dt| < 3\text{nT/hr}^{-1}$, Olsen et al (2014)
- Merging electric field at the magnetopause $E_m < 0.8\text{mVm}^{-1}$, Olsen et al (2014)
- Interplanetary Magnetic Field (IMF) $B_z > 0\,\text{nT}$ and $|B_y| < 10\,\text{nT}$

where the latter two conditions are based on two hourly means of 1 min values from the OMNI data-base, `http://omniweb.gsfc.nasa.gov`, prior to the data timestamp.

Observed field GVO estimates are derived from sums and differences (along-track and also across track in the case of *Swarm* Alpha and Charlie) of the

selected data, taking all data falling within 700 km of the GVO target location during the specified time window (1 or 4 months), fitting these by a local potential and then using this potential to estimate the vector field at the target location.

Core field GVO estimates are derived in the 1 monthly case by applying Principle Component Analysis (Cox et al, 2018) denoising to identify and remove local time and obvious external signals, then performing an epoch-by-epoch spherical harmonic analysis to identify and remove as far as possible remaining external and toroidal fields. For the 4 monthly datafiles, a-priori estimates of the magnetopheric field and associated induced field from the CHAOS model (Olsen et al, 2006; Finlay et al, 2020) and the ionospheric field and associated induced field from the CM4 model (Sabaka et al, 2004) were removed from the satellite data prior to fitting the potential and then epoch-by-epoch spherical harmonic analysis was applied to identify and remove remaining external and toroidal fields. Identical data selection and processing steps were applied to the *Swarm*, CHAMP and Cryosat-2 data (for a more detailed description of the algorithm, see Hammer et al, 2020a).

The GVO datasets for *Swarm*, CHAMP and Cryosat-2 have been archived online at:

`http://www.spacecenter.dk/files/magnetic-models/GVO/GVO_data_SWARM.zip`
`http://www.spacecenter.dk/files/magnetic-models/GVO/GVO_data_CHAMP.zip`
`http://www.spacecenter.dk/files/magnetic-models/GVO/GVO_data_CRYOSAT2.zip`

Each zip file contains the GVO datafiles (1 monthly or 4 monthly cadence) in the same .cdf format Hammer et al (2020c) along with a readme file summarizing the satellite data sources, selection criteria and processing steps applied. Filenames are of the form $YY\_OPER\_VOBS\_XM\_2\_\_20131215T000000\_20200315T000000\_0101.cdf$ where YY indicates the satellite (SW for *Swarm*, CH for CHAMP, CR for Cryosat-2) and X is either 1 or 4 indicating 1 monthly or 4 monthly cadence respectively. The variables provided in the .cdf file are Timestamp for the GVO field estimate; Geocentric Latitude (degrees); Geocentic Longitude (degrees); Geocentric Radius (km); GVO estimate of observed field (nT) including all sources; Error estimate of observed field GVO (nT), derived from the misfit to the contributing data; GVO estimate of Core field(nT), where selection and de-noising has been applied to isolate the core field as far as possible; Error estimate of core field GVO (nT) based on comparison to the CHAOS field model, Timestamp for SV, GVO Core Field Secular Variation (SV) Estimate (nT/yr) derived from annual differences of the GVO estimate of Core field, and Error estimates for Core field SV GVO (nT/yr) again based on comparisons with the CHAOS field model.

To illustrate the GVO secular variation time series, Figure 2.2 presents composite GVO time series for the radial, southward and eastward field components, mapped from their nominal altitude to 700 km using the CHAOS-7.2 field model in order to aid visualization.

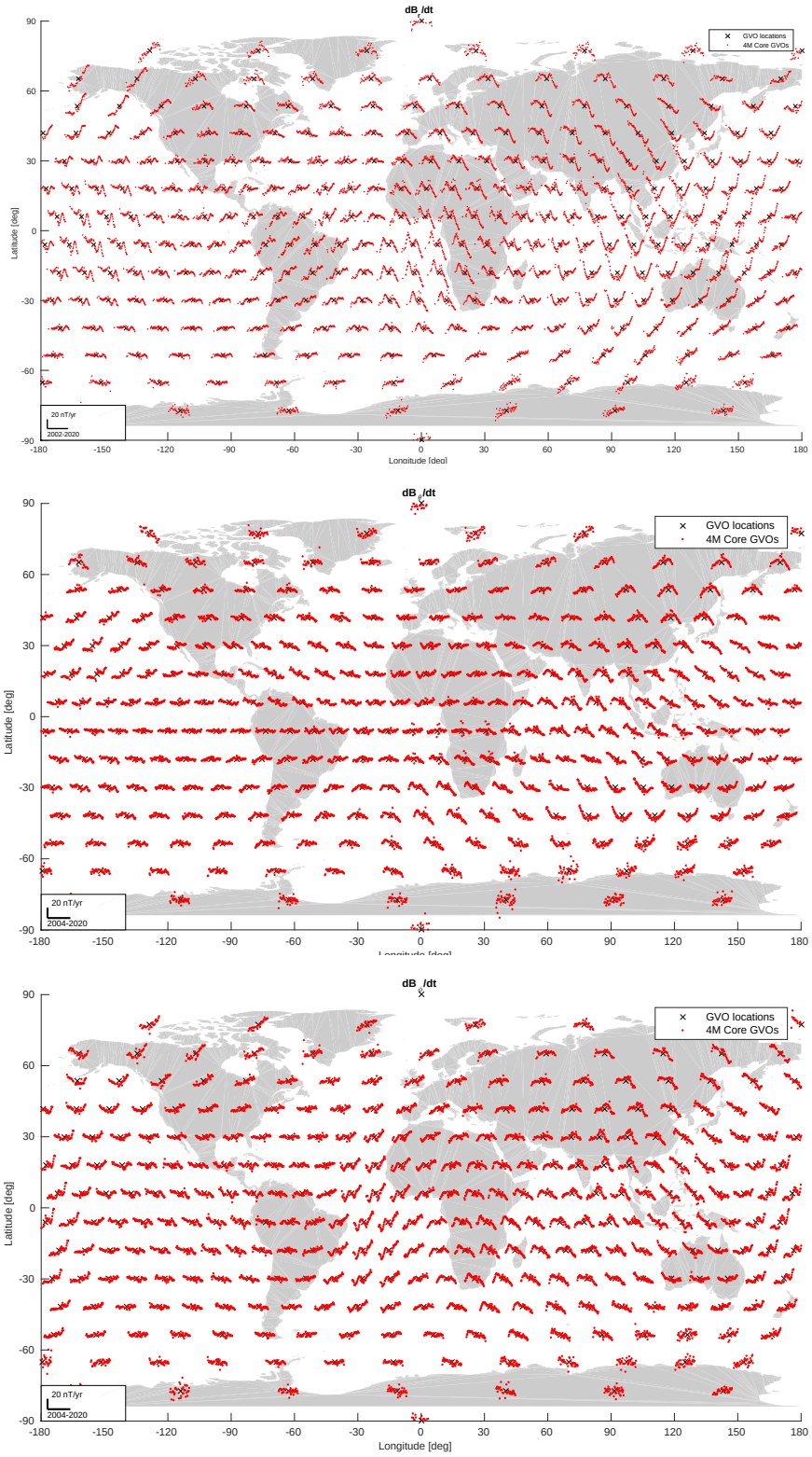

Figure 2.2: Composite GVO time-series of 4-monthly values of dB_r/dt (top), dB_θ/dt (middle) and dB_ϕ/dt (bottom) from CHAMP, Cryosat-2 and *Swarm*. For visualization this has been mapped to a common altitude of 700 km.

Table 2.1 below presents for comparison the start time, end time, altitude, number of GVOs, data cadence, and mean estimated uncertainties for the observed field and core field GVOs from *Swarm*, CHAMP and Cryosat-2.

Table 2.1: Characteristics of GVO datasets from *Swarm*, CHAMP and Cryosat-2. σ^{Obs} denotes the mean over all GVO locations of the estimated uncertainties on the observed field GVOs, derived from their misfit to the contributing satellite data, σ^{SV} denotes the mean over all GVO locations of the supplied uncertainties on the core field SV, derived using comparisons to the CHAOS-7 field model.

	Start date	End date	Altitude [km]	GVOs	Cadence [months]	$\sigma^{Obs}_{B_r}$ [nT]	$\sigma^{Obs}_{B_\theta}$ [nT]	$\sigma^{Obs}_{B_\phi}$ [nT]	$\sigma^{SV}_{B_r}$ [nT/yr]	$\sigma^{SV}_{B_\theta}$ [nT/yr]	$\sigma^{SV}_{B_\phi}$ [nT/yr]
Swarm	2013.12.15	2020.03.15	490	300	1	4.17	7.18	6.92	1.62	1.66	1.32
Swarm	2014.03.01	2020.03.01	490	300	4	1.77	3.35	2.77	1.27	1.41	2.28
CHAMP	2000.08.15	2010.09.15	370	300	1	5.13	8.33	7.69	4.53	5.38	6.50
CHAMP	2001.03.01	2010.07.01	470	300	4	2.30	3.87	3.02	2.11	1.81	1.79
Cryosat-2	2010.07.01	2018.11.01	727	300	4	4.47	6.47	5.20	3.49	4.00	3.04

2.3 An update of the CHAOS field model and delivery of related datasets

The CHAOS (CHAMP, Ørsted, and *Swarm*) geomagnetic field model (Olsen et al, 2006, 2014; Finlay et al, 2020) is a time-dependent spherical harmonic model of the near-Earth geomagnetic field that aims to represent the internal field to high resolution in space and time. It has been developed at DTU over the past 15 years and is fitted directly to satellite data in the magnetometer frame, using vector field data (and along and cross track field differences) at non-polar latitudes and scalar data (and along and cross track differences) at polar latitudes, using data from dark and geomagnetically quiet time and co-estimating near-Earth magnetospheric sources. With support in part from the 4D Earth project it has recently been updated to CHAOS-7 using data the latest *Swarm* dta, as well as platform magnetometer from the Cryosat-2 mission whose use was made possible by co-estimating magnetometer calibration parameters (Finlay et al, 2020).

2.3.1 Satellite data

Here we provide details of the satellite data used to derive the latest update of the CHAOS model, CHAOS-7.3. These have been extracted for delivery as part of the 4D Earth project. Histograms showing the various data sets contributing to CHAOS-7.3 are presented in Fig. 2.3.

A .zip file containing the various satellite data used in building CHAOS-7.3, labelled by data mission and type is available at:

`http://www.spacecenter.dk/files/magnetic-models/CHAOS-7/CHAOS-7_3_data.zip`

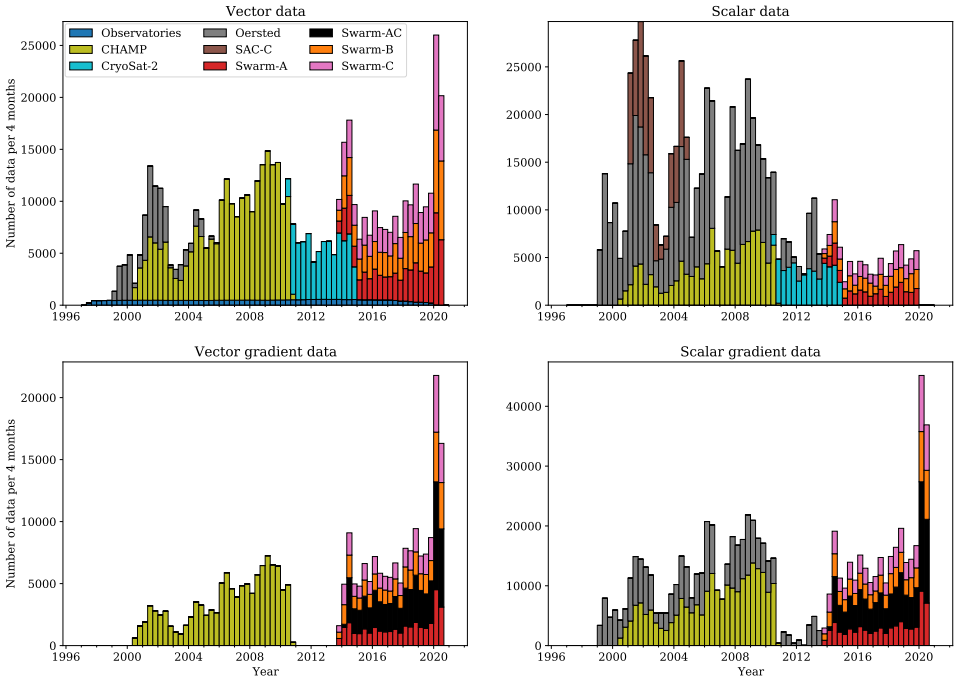

Figure 2.3: Histograms showing number of data of difference types used to construct the CHAOS-7.3 geomagnetic field model.

Table 2.2: Characteristics of CHAOS-7.3 satellite datasets, vector field.

	Start date	End date	Mean Altitude [km]	No. triples	rms misfit, CHAOS-7.3 B_r [nT]	B_θ [nT]	B_ϕ [nT]
Ørsted	1999.03.16	2005.12.06	756	48109	4.03	4.68	4.76
CHAMP	2000.07.27	2010.09.03	357	227145	1.71	2.35	1.95
Cryosat-2	2010.08.01	2014.12.27	728	71151	4.98	6.00	6.67
Swarm A,B,C	2013.11.26	2020.07.20	473	197443	1.49	3.16	1.96

Table 2.3: Characteristics of CHAOS-7.3 satellite datasets, scalar field.

	Start date	End date	Mean Altitude [km]	No. triples	rms misfit, CHAOS-7.3 F [nT]
Ørsted	1999.03.15	2013.06.25	750	352232	2.23
CHAMP	2000.07.27	2010.09.03	357	227145	1.71
SAC-C	2001.01.23	2004.12.03	711	76104	2.96
Cryosat-2	2010.08.01	2014.12.30	726	48679	7.66
Swarm A,B,C	2013.11.26	2019.12.31	474	80190	3.42

2.3.2 Ground observatory data

Here we provide brief details of the ground observatory data set used in CHAOS-7.3, that has also been extracted and delivered as part of the 4D Earth project.

Annual differences of revised observatory monthly means (Olsen et al, 2014) for the time interval January 1997 to July 2020 were used to provide additional constraints on the secular variation. Revised monthly means were derived from the hourly mean values at the 183 observatories shown in Fig. 2.4 (including 11 with minor site changes during the considered time interval) which were checked for trends, spikes and other errors (Macmillan and Olsen, 2013). Monthly means were calculated by a robust method based on Huber weights (Huber, 2004), from all local times at all latitudes. We removed estimates of the ionospheric (plus induced) field as predicted by the CM4 model (Sabaka et al, 2004) and the large-scale magnetospheric (plus induced) field, predicted by a preliminary field model, CHAOS-7.2.

A .zip file containing the ground observatory revised monthly mean data as used to build CHAOS-7.3 has been made available at:

`http://www.spacecenter.dk/files/magnetic-models/GOBS/GO_V33_1monthly.zip`

A version of the ground observatory data, based on the same hourly mean data but with revised means computed over 4 month windows is available at:

`http://www.spacecenter.dk/files/magnetic-models/GOBS/GO_V33_4monthly.zip`

Finally a version of the ground observatory data, based on the same hourly mean data but computing simple annual means to allow comparison with historical observatory annual means, is available at:

`http://www.spacecenter.dk/files/magnetic-models/GOBS/GO_V33_1yr.zip`

Examples of one monthly revised monthly means, with the CHAOS-7.3 model shown for reference are presented in Fig. 2.5.

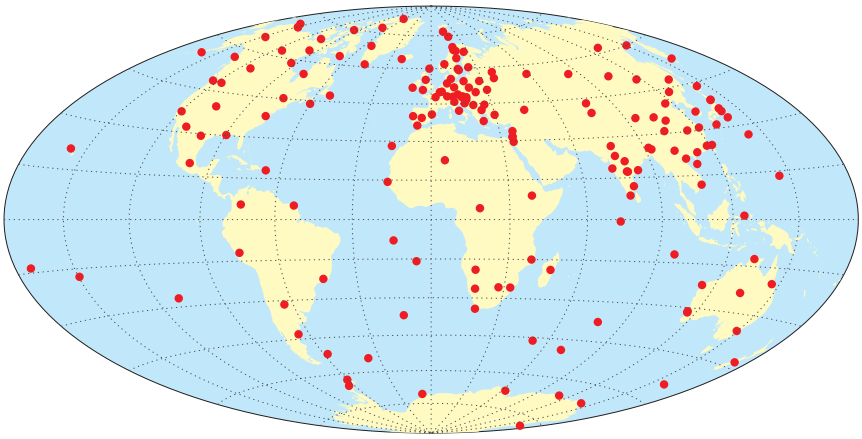

Figure 2.4: Map showing positions of ground observatories. IAGA codes for the stations are: AAA0, AAE1, ABG0, ABG1, ABK0, AIA0, ALE0, AMS0, AMT0 , API0 , API2, AQU0, ARS0, ASC0, ASP0, BDV0, BEL0, BFE0, BFO0, BGY1, BJN1, BLC0, BMT1, BNG0, BOU0, BOX0, BRW0, BSL0, BSL1, CBB0, CBI0, CDP0, CDP2, CKI0, CLF0, CMO3, CNB0, CNH3, COI0, CPL0, CSY0, CSY1, CTA0, CTS0, CYG0, CZT0, DED0, DLR0, DLT0, DOB1, DOU0, DRV0, EBR0, ELT0, ESA0, ESK0, EYR0, FCC0, FRD0, FRN0, FUQ0, FUR0, GAN0, GCK0, GDH2, GLM0, GNA0, GNG0, GUA0, GUI0, GUI3, GZH2, HAD0, HBK0, HER0, HLP0, HON3, HRB0, HRN0, HTY0, HUA0, HYB0, IPM0, IQA0, IQA1, IRT2, IZN0, JAI0, JCO0, KAK0, KDU0, KEP0, KHB0, KIR0, KIV2, KMH0, KMH1, KNY0, KNZ0, KOU0, KSH0, KSH1, LER0, LIV0, LMM0, LNP0, LON0, LOV0, LRM0, LRV0, LVV2, LYC0, LZH1, MAB0, MAW0, MBO0, MCQ0, MEA0, MGD0, MIZ0, MMB0, MNK0, MOS0, MZL0, NAQ0, NCK0, NEW0, NGK0, NGP1, NMP1, NUR0, NVS0, OTT0, PAF2, PAG0, PBQ0, PEG2, PET2, PHU0, PHU1, PIL0, PND0, PPT0, PST0, QGZ1, QIX0, QIX1, QSB0, QZH0, RES0, SBA0, SBL0, SFS2, SHE0, SHL0, SHU0, SIL0, SIT2, SJG2, SOD3, SPT0, SSH0, STJ0, SUA0, SUA, TAM0, TAN0, TDC0, TEO0, TFS0, THJ0, THL0, THY0, TIR0, TIR1, TND0, TRO0 , TRW0, TSU0, TUC2, UJJ0, UPS0, VAL0, VIC0, VNA0, VSK0, VSK1, VSS0, WHN0, WIC0, WIK0, WNG0, YAK1, YKC2.

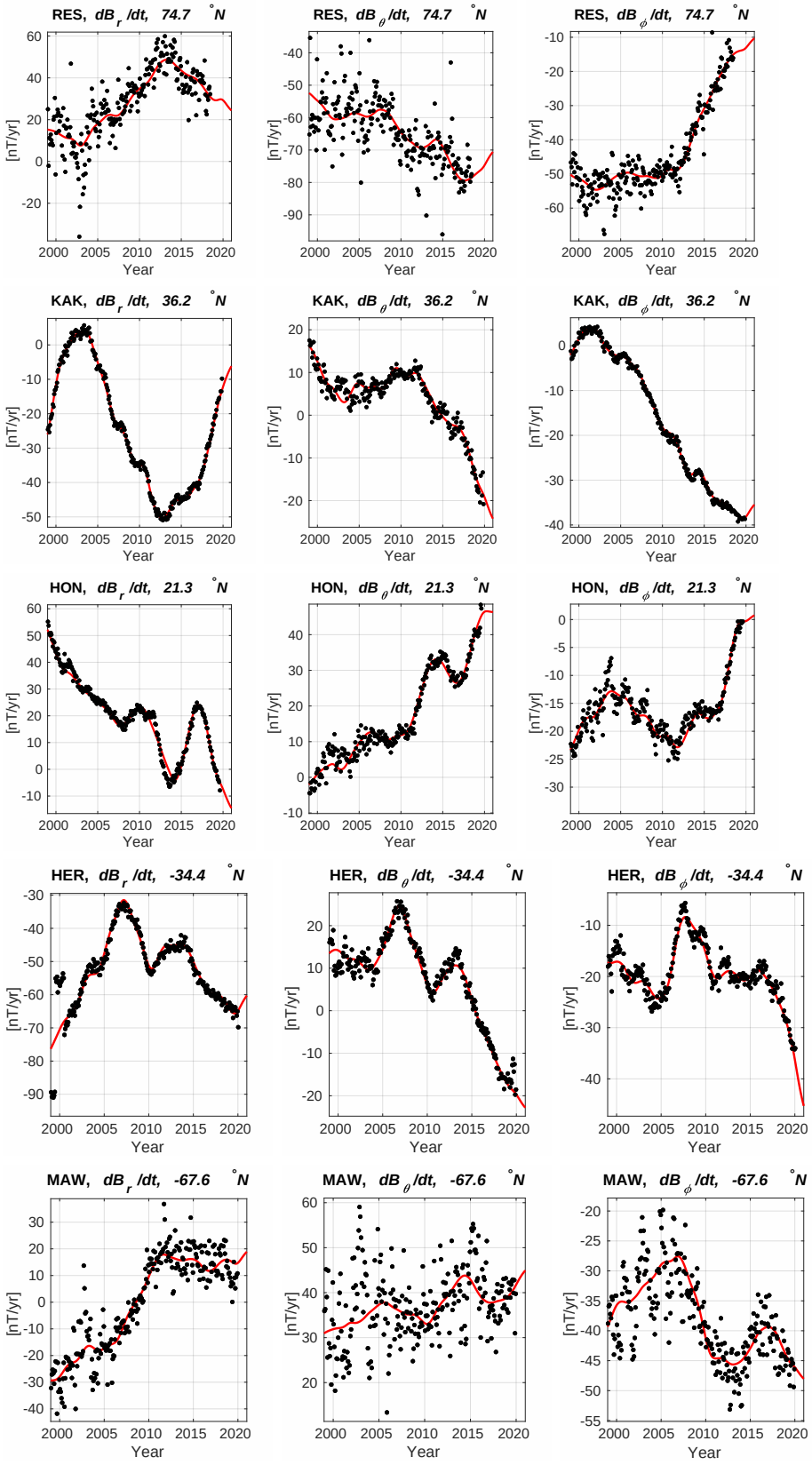

Figure 2.5: Fit of the CHAOS-7.3 model (red line) to secular variation data, annual differences of revised monthly means (black dots), at example ground observatories.

2.3.3 The CHAOS-7.3 model

The CHAOS-7.3 model was derived in August 2020 using the modelling approach as for CHAOS-7 (Finlay et al, 2020) but with updated *Swarm* and ground observatory data and slightly increased regularization of time-dependent core field and much stronger regularization of the Cryosat-2 s_1 magnetometer sensitivities. Details of the model parameterization is given in Table 2.4.

Table 2.4: Summary of parameters defining the model setup in CHAOS-7.3.

Setup Parameter	Description	
N_{tdep}	Maximum SH degree of time-dependent internal field	20
J	Order of B-Splines	6
Δt_k	B-spline knot spacing	0.5 yr
t_{start}	Start time of spline basis	1997.1
t_{end}	End time of spline basis	2021.1
N_{int}	Maximum SH degree of static internal field	185
N_{SM}	Maximum SH degree of SM external field	2
ΔT_{SM1}	Bin size for degree 1 SM offsets	30 days
N_{GSM}	Maximum SH degree of GSM external field	2 (only $m = 0$ terms)
$\Delta T_{\mathrm{Euler}}$	Bin size for Euler angle determination	10 days
ΔT_{CAL}	Bin size for calibration parameters	21 days

The time-dependent internal field part of CHAOS-7.3 model has been archived in .mat, .shc and in spline coefficient formats at:

`http://www.spacecenter.dk/files/magnetic-models/CHAOS-7/CHAOS-7.3.mat`
`http://www.spacecenter.dk/files/magnetic-models/CHAOS-7/CHAOS-7.3_core.shc`
`http://www.spacecenter.dk/files/magnetic-models/CHAOS-7/CHAOS-7.3_spline-coeffi`

The latest version of the *chaosmagpy* python forward package, that can be used to evaluate CHAOS-7.3, is available from

`https://pypi.org/project/chaosmagpy/`

Fig. 2.6 below shows maps of the radial component of the magnetic field, and its first and second time-derivatives (the secular variation and secular acceleration) downward continued to the core-mantle boundary in 2020.0. Note the enhanced amplitudes of secular variation and secular acceleration at low latitudes and in the northern polar region. Fig. 2.7 presents time series of the secular variations of selected spherical harmonic coefficients, along with two other recent models constructed with different modelling methods, CM6 (Sabaka et al, 2020) and model MCO_SHA_2Y, an early model derived using the approach of Ropp et al (2020).

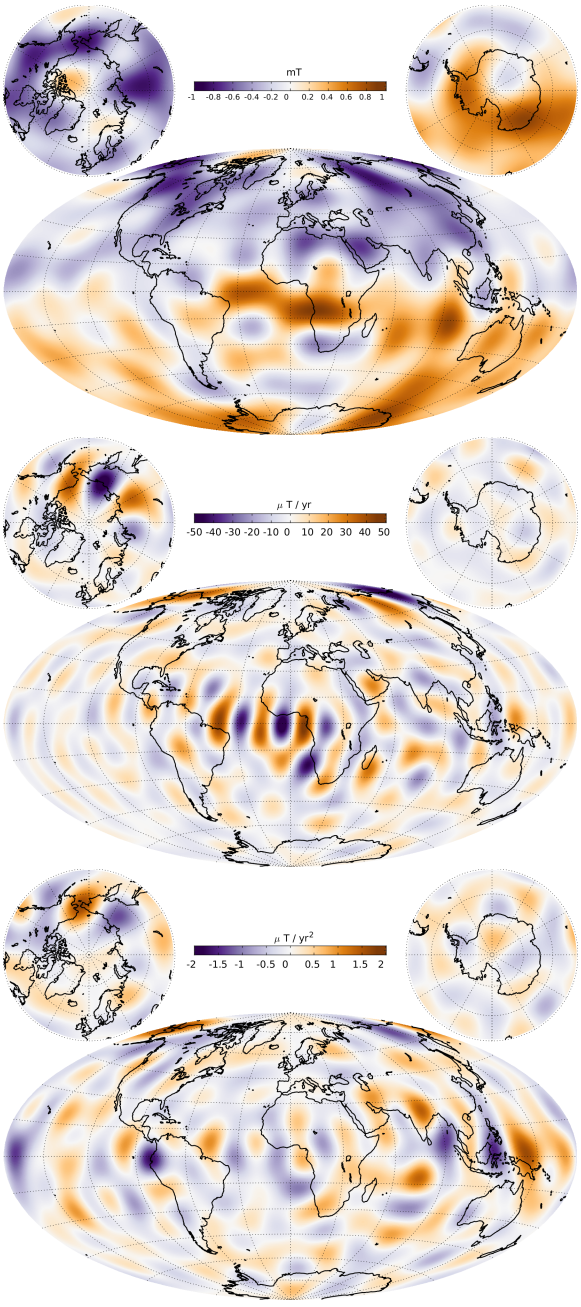

Figure 2.6: Maps from CHAOS-7.3 of the radial magnetic field (MF, top row), its first time derivative (SV, middle row) and second time derivative (SA, bottom row) at the core-mantle boundary in 2020.0, Truncation degrees are 13, 17 and 15 respectively for the MF, SV and SA.

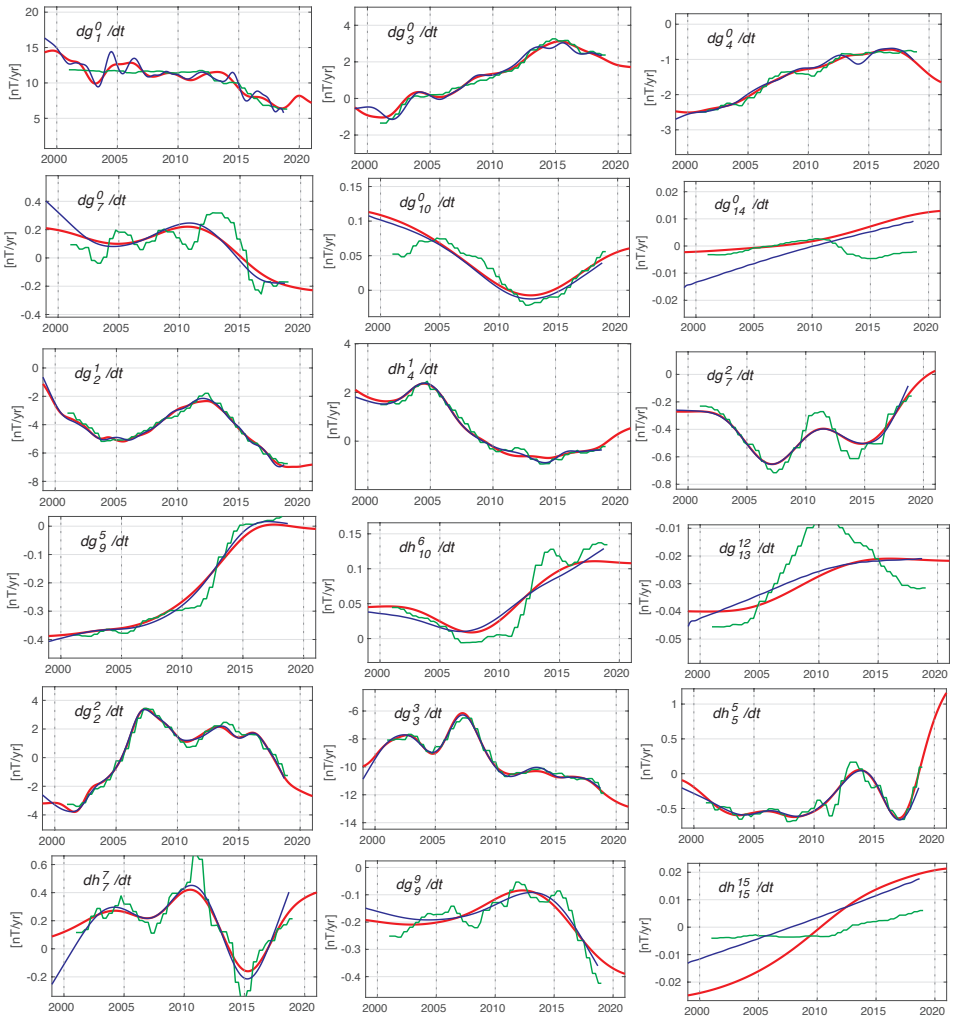

Figure 2.7: Time-dependence of example spherical harmonic coefficients of the internal field SV from CHAOS-7.3 (solid red line). Also shown are the CM6 model of Sabaka et al (2020)(blue line) and model MCO_SHA_2Y, an early model derived using the approach of Ropp et al (2020) (green line). Top two rows are zonal coefficients, bottom two rows are sectoral coefficients, middle two rows are tesseral coefficients.

2.4 Summary

This report has described initial deliveries for the 4D Deep Earth:Core project of GVO datasets from *Swarm*, CHAMP and Cryosat-2, constructed using identical processing schemes; an update of the CHAOS field model to version 7.3 using the latest *Swarm* and ground observatory data, and related satellite and ground observatory datasets. These constitute delivery D-B.1 by DTU.

Links to all the datafiles described above will be available on the 4D Earth webpage:

`https://4d-earth-swarm.univ-grenoble-alpes.fr/`

Bibliography

Cox G, Brown WJ, Billingham L, Holme R (2018) MagPySV: A Python package for processing and denoising geomagnetic observatory data. Geochemistry, Geophysics, Geosystems 19(9):3347–3363

Finlay CC, Kloss C, Olsen N, Tøffner-Clausen L, Grayver A, Kuvshinov A (2020) The CHAOS-7 geomagnetic field model and observed changes in the South Atlantic Anomaly. Earth Planets Space 72, DOI 10.1186/s40623-020-01252-9

Hammer MD, Cox GA, Brown WJ, Beggan C, Finlay CC (2020a) Geomagnetic Virtual Observatories: Monitoring geomagnetic secular variation with the Swarm satellites. Earth Planets Space xx:(in prep)

Hammer MD, Cox GA, Brown WJ, Beggan C, Finlay CC (2020b) Swarm data, innovation, and science cluster, geomagnetic virtual observatory project: Description of algorithm. Available at `http://www.spacecenter.dk/files/magnetic-models/GVO/GVO_Product_Algorithm.pdf`(2020/09/14)

Hammer MD, Cox GA, Brown WJ, Beggan C, Finlay CC (2020c) Swarm data, innovation, and science cluster, geomagnetic virtual observatory project: Product definition document. Available at `http://www.spacecenter.dk/files/magnetic-models/GVO/GVO_Product_Definition.pdf`(2020/09/14)

Hammer MD, Cox GA, Brown WJ, Beggan C, Finlay CC (2020d) Swarm data, innovation, and science cluster, geomagnetic virtual observatory project: Validation document. Available at `http://www.spacecenter.dk/files/magnetic-models/GVO/GVO_Validation.pdf`(2020/09/14)

Huber PJ (2004) Robust statistics. Wiley

Leopardi P (2006) A partition of the unit sphere into regions of equal area and small diameter. Electronic Transactions on Numerical Analysis 25(12):309–327

Macmillan S, Olsen N (2013) Observatory data and the Swarm mission. Earth, Planets and Space 65:1355–1362

Mandea M, Olsen N (2006) A new approach to directly determine the secular variation from magnetic satellite observations. Geophys Res Lett 33:L15,306, DOI 10.1029/2006GL026616

Olsen N, Mandea M (2007) Investigation of a secular variation impulse using satellite data: The 2003 geomagnetic jerk. Earth Planet Sci Lett 255:94–105, DOI 10.1016/j.epsl.2006.12.008

Olsen N, Lühr H, Sabaka TJ, Mandea M, Rother M, Tøffner-Clausen L, Choi S (2006) CHAOS – a model of Earth's magnetic field derived from CHAMP, Ørsted, and SAC-C magnetic satellite data. Geophys J Int 166:67–75, DOI 10.1111/j.1365-246X.2006.02959.x

Olsen N, Lühr H, Finlay CC, Tøffner-Clausen L (2014) The CHAOS-4 Geomagnetic Field Model. Geophys J Int 1997:815–827

Olsen N, Albini G, Bouffard J, Parrinello T, Tøffner-Clausen L (2020) Magnetic observations from CryoSat-2: calibration and processing of satellite platform magnetometer data. Earth, Planets and Space 72

Reigber C, Lühr H, Schwintzer P, Wickert J (2005) Earth Observation with CHAMP, Results from Three Years in Orbit. Springer Verlag, Berlin

Ropp G, Lesur V, Baerenzung J, Holschneider M (2020) Sequential modelling of the earth's core magnetic field. Earth, Planets and Space (in press)

Sabaka TJ, Olsen N, Purucker ME (2004) Extending comprehensive models of the Earth's magnetic field with Ørsted and CHAMP data. Geophys J Int 159:521–547, DOI 10.1111/j.1365-246X.2004.{02421}.x

Sabaka TJ, Tøffner-Clausen L, Olsen N, Finlay CC (2020) CM6: A comprehensive geomagnetic field model derived from both champ and swarm satellite observations. Earth, Planets and Space 72, DOI 10.1186/s40623-020-01210-5

Chapter 3

Long time series of outputs from a geodynamo model approaching Earth's core conditions

4DEarth_Swarm_Core ESA project deliverable D-C.1

J. Aubert
IPG Paris

3.1 General description

This document refers to publicly available output data from a geodynamo simulation that approaches closely to the physical conditions of Earth's core. In the model parameter space, this model is part of a series that defines a path connecting the conditions where classical dynamo models are found to those of the Earth's core. The theoretical definition of this path may be found in Aubert et al (2017), and the model described here is located at 71% of this path (path parameter $\epsilon = 10^{-5}$). The outputs that are made available here consist in coefficients describing the poloidal magnetic field outside the core, the diffusive part of the poloidal magnetic field temporal rate-of-change (the secular variation), and the coefficients describing the velocity field at the core surface. The model operates with stress-free boundary conditions, which implies that Ekman boundary layers are not described and that the core surface directly corresponds to the free stream. Table 3.1 lists the key time scales and associated dimensionless numbers of this model together with those expected at Earth's core conditions.

From the dimensionless outputs of the numerical model, the values of the velocity and magnetic field coefficients presented in the data file are **already scaled to dimensional values**, in nanoteslas for the magnetic field, nanoteslas per year for the diffusive part of the secular variation, and kilometers per year for the velocity field. Here I mention some details for the re-scaling procedure that has been applied. Re-scaling can be done in a completely self-consistent manner only once the model conditions reach those of the Earth's core. The path theory serves to rescale these quantities in a way that rationalizes the gap that still exists between those two conditions (Aubert, 2018, 2020). For the time series presented here, the time basis is provided by the choice of the magnetic diffusivity η in table 3.1. From there and

Quantity	Definition	71% of path model	Earth's core
Earth radius	a	6371.2 km	6371.2 km
core surface radius	r_o	3485 km	3485 km
outer core thickness	D	2260 km	2260 km
magnetic diffusivity	η	1.2 m^2/s	$\approx$ 1.2 m^2/s
magnetic diffusion time	$\tau_\eta = D^2/\eta$	135000 yr	$\approx$ 135000 yr
planetary rotation period	$2\pi\tau_\Omega = 2\pi/\Omega$	12 days	1 day
Alfvén time	$\tau_A = \sqrt{\rho\mu}D/B$	5.8 yr	$\approx$ 2 yr
1D Alfvén speed	$D/\sqrt{3}\tau_A$	225 km/yr	$\approx$ 650 km/yr
core overturn time	$\tau_U = D/U$	118 yr	$\approx$ 120 yr
1D convective speed	$D/\sqrt{3}\tau_U$	11 km/yr	$\approx$ 11 km/yr
Magnetic Ekman number	$E/Pm = \tau_\Omega/\tau_\eta$	3.8 10^{-8}	$\approx$ 3.2 10^{-9}
Magnetic Reynolds number	$Rm = \tau_\eta/\tau_U$	1140	$\approx$ 1100
Lundquist number	$S = \tau_\eta/\tau_A$	23300	$\approx$ 68000

Table 3.1: Key parameters for the model, presented together with their model values and values expected at Earth's core conditions. B and U are root-mean-squared amplitudes of the magnetic field inside the simulated core.

the value of the magnetic Reynolds number Rm immediately follow the determination of the core overturn time τ_U involving the root-mean-squared flow velocity U in the shell and the re-scaling of the velocity field. The value of the Lundquist number gives access to the Alfvén time τ_A, which however differs from its target Earth value as we are not yet at the end of the path. The r.m.s dimensional magnetic field amplitude B can therefore be obtained by considering that the density ρ of the simulated fluid shell is $(5.8/2)^2$ time stronger than its Earth counterpart $\rho = 11000\,\mathrm{kg/m^3}$, this former factor accounting for the differences in the model and Earth Alfvén times.

Figure 3.1 presents temporal sequences of the core-mantle boundary secular acceleration energy (as defined in Aubert, 2018) and Earth-surface jerk energy (as defined in Aubert and Finlay, 2019). The sequence contained in the data files starts at timestamp 4200 years. The preceding temporal sequence is not proposed as it contains a number of changes in model resolution, output resolution, time step that have followed from the need to tackle numerical instabilities and from discussions within the consortium, which make this earlier part of the model unsuitable for public release. The duration of the released sequence is currently 8811.3 years. The numerical time step used for the computation is 0.3 hours. Outputs have been recorded at a sampling rate of 30 hours. The sampling rate selected for public release is 0.2 years. The consortium is free to discuss whether a faster delivery sampling rate is needed, but it should be kept in mind that this comes at the cost of file size. Furthermore, we have previously shown (Aubert, 2018) that the signal contains almost no energy at periods shorter than the planetary rotation period

Jerk No.	timestamp (years)
1	4600
2	5750
5	6490
6	7300
7	7620
8	7840
9	8880
10	9673
11	10590
12	12620

Table 3.2: Approximate timestamps for notable jerks in the publicly available part of the sequence.

$2\pi\tau_\Omega$ = 283 hours = 11.8 days = 0.03 years. The time stamps for notable jerk events are reported in table 3.2.

3.2 Data format and description

The file format is MATLAB `.mat`.

3.2.1 Magnetic field coefficients

To describe the magnetic field at and above the core surface, we adopt the classical Gauss coefficient description for the magnetic field. Denoting the colatitude as θ and the Greenwich-centered longitude as φ, the poloidal field at a radius r above the core-mantle boundary may be written

$$\mathbf{B}_{\boldsymbol{p}}(r,\theta,\varphi,t) = -\boldsymbol{\nabla} V \tag{3.1}$$

where

$$V(r,\theta,\varphi,t) = a\sum_{l=1}^{30}\left(\frac{a}{r}\right)^{l+1}\sum_{m=0}^{l}\left[g_l^m(t)\cos m\varphi + h_l^m(t)\sin m\varphi\right]P_l^m(\cos\theta). \tag{3.2}$$

Here t is time, a = 6371.2 km is Earth's magnetic radius of reference, P_l^m is the Schmidt-seminormalised Legendre function of degree l and order m.

The file `gauss_Bsurf.mat` comprises the dimensional timestamp vector `timers` containing the discrete values of t and an array `gnm` containing the coefficients $g_l^m(t)$, $h_l^m(t)$ arranged according to:

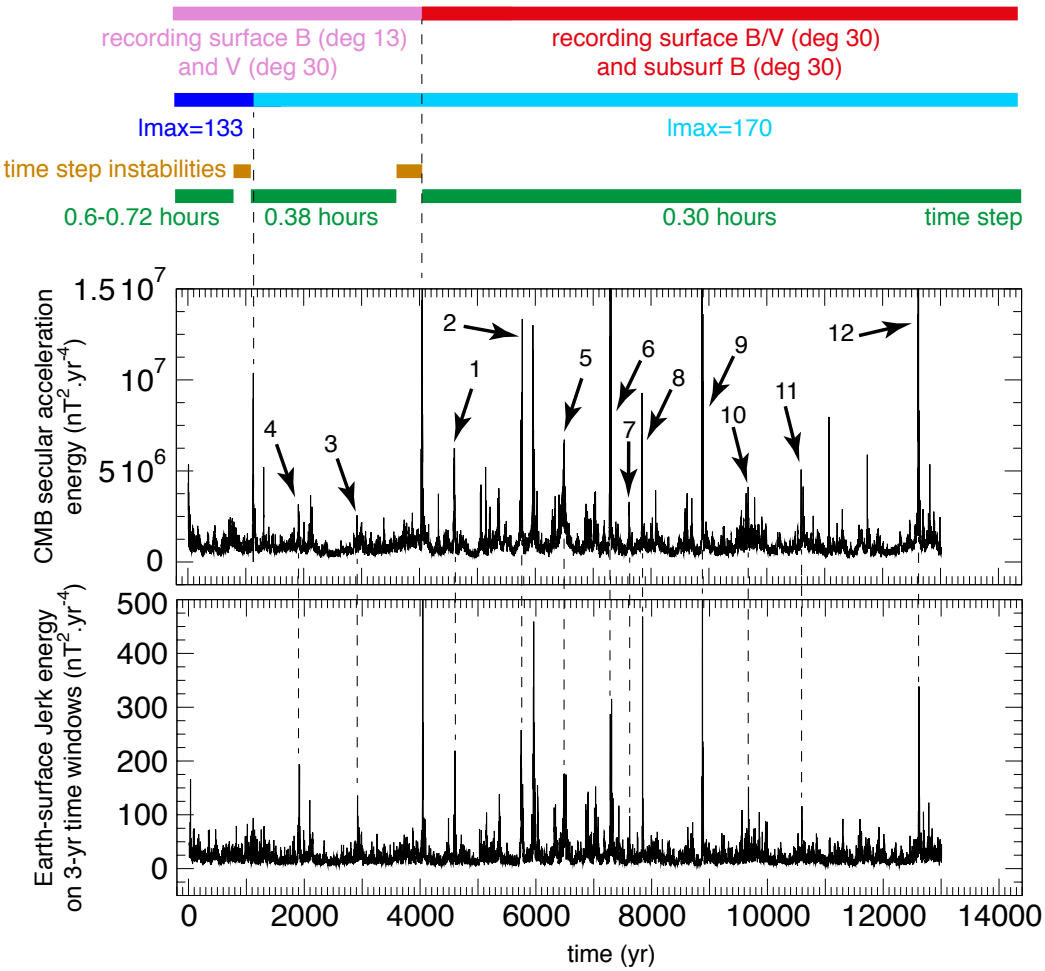

Figure 3.1: Core-mantle boundary (CMB) secular acceleration energy (top) and Earth-surface jerk energy (bottom), as functions of the dimensional simulation time. See Aubert (2018); Aubert and Finlay (2019) for definitions. The outputs have been truncated here at spherical harmonic degree and order 13 (which is the minimum spatial resolution for outputs of the whole sequence), but the publicly available outputs are supplied up to a higher spherical harmonic resolution of 30. The colored bands above the graphs locate notable events in the simulation concerning the nature and maximum spherical harmonic degree of outputs (pink/red), the native spherical harmonic degree $\ell_{\max}$ of the computation (blue/cyan), the computation time step values (green) and encountered instabilities thereof (brown).

$$
\begin{aligned}
\texttt{gnm}(:,1) &= g_1^0(t)\\
\texttt{gnm}(:,2) &= g_1^1(t)\\
\texttt{gnm}(:,3) &= h_1^1(t)\\
\texttt{gnm}(:,4) &= g_2^0(t)\\
\texttt{gnm}(:,5) &= g_2^1(t)\\
\texttt{gnm}(:,6) &= h_2^1(t)\\
\texttt{gnm}(:,7) &= g_2^2(t)\\
\texttt{gnm}(:,8) &= h_2^2(t)\\
&\ldots\\
\texttt{gnm}(:,959) &= g_{30}^{30}(t)\\
\texttt{gnm}(:,960) &= h_{30}^{30}(t)
\end{aligned}
$$

Note that the sinus coefficients corresponding to $m = 0$ are not stored as they vanish identically. There are therefore 960 coefficients corresponding to a description of the output up to spherical harmonic degree and order 30. The core surface poloidal magnetic field is then obtained by setting r to $r_o = 3485$ km in equation (3.2).

In file `gauss_Magdiff.mat` the Gauss coefficients corresponding to the diffusive part $\eta\nabla^2\mathbf{B}_p$ of the secular variation $\partial\mathbf{B}_p/\partial t$ below the core surface are encoded in the variable `dgnm` together with the time stamp `timers`. The advective part of the secular variation can then be obtained by taking the centered finite differences of variable `gnm` from file `gauss_Bsurf.mat` and subtracting `dgnm` to the result. The magnetic diffusion obviously does only make sense at the core surface i.e. by setting r to $r_o = 3485$ km in equation (3.2), but its representation in terms of the same Gauss coefficients as those used for the poloidal field allows to quickly apprehend its contribution to the total secular variation, and also to quickly convert the output to a radial magnetic field, which is the representation that is usually preferred to cast the magnetic induction equation at the core surface.

3.2.2 Velocity field coefficients

The core surface velocity field coefficients are described using the spheroidal-toroidal formalism. The θ and φ components of the core surface velocity vector $\mathbf{u}$ are written

$$
\mathbf{u} = \begin{pmatrix} u_\theta = \dfrac{1}{\sin\theta}\dfrac{\partial T}{\partial \varphi} + \dfrac{\partial S}{\partial \theta} \\ u_\varphi = -\dfrac{\partial T}{\partial \theta} + \dfrac{1}{\sin\theta}\dfrac{\partial S}{\partial \varphi} \end{pmatrix} \tag{3.3}
$$

The spectral decomposition of T, S obeys

$$T = \sum_{l=1}^{30} \sum_{m=0}^{l} \left[tc_l^m(t) \cos m\varphi + ts_l^m(t) \sin m\varphi \right] P_l^m(\cos\theta) \tag{3.4}$$

$$S = \sum_{l=1}^{30} \sum_{m=0}^{l} \left[sc_l^m(t) \cos m\varphi + ss_l^m(t) \sin m\varphi \right] P_l^m(\cos\theta) \tag{3.5}$$

The file `gauss_Vsurf.mat` contains the timestamp `timers` together with two arrays `tnm` and `snm` where the coefficients tc_l^m,ts_l^m and sc_l^m,ss_l^m are respectively stored. The ordering follows that of the magnetic field Gauss coefficients i.e.

$$\begin{aligned}
\texttt{tnm}(:,1) &= tc_1^0(t) \\
\texttt{tnm}(:,2) &= tc_1^1(t) \\
\texttt{tnm}(:,3) &= ts_1^1(t) \\
\texttt{tnm}(:,4) &= tc_2^0(t) \\
\texttt{tnm}(:,5) &= tc_2^1(t) \\
\texttt{tnm}(:,6) &= ts_2^1(t) \\
\texttt{tnm}(:,7) &= tc_2^2(t) \\
\texttt{tnm}(:,8) &= ts_2^2(t) \\
&\dots \\
\texttt{tnm}(:,959) &= tc_{30}^{30}(t) \\
\texttt{tnm}(:,960) &= ts_{30}^{30}(t)
\end{aligned}$$

Note that the sinus coefficients corresponding to $m = 0$ are not stored as they vanish identically. As for the magnetic field coefficients above there are 960 coefficients for each scalar, corresponding to a description of the output up to spherical harmonic degree and order 30.

Links to all the datafiles described above will be available on the 4D Earth webpage:

`https://4d-earth-swarm.univ-grenoble-alpes.fr/`

Bibliography

Aubert J (2018) Geomagnetic acceleration and rapid hydromagnetic wave dynamics in advanced numerical simulations of the geodynamo. Geophys J Int 214(1):531–547

Aubert J (2020) Recent geomagnetic variations and the force balance in Earth's core. Geophys J Int DOI 10.1093/gji/ggaa007, doi: 10.1093/gji/ggaa007

Aubert J, Finlay CC (2019) Geomagnetic jerks and rapid hydromagnetic waves focusing at Earth's core surface. Nature Geosci 12(5):393–398, DOI 10.1038/s41561-019-0355-1

Aubert J, Gastine T, Fournier A (2017) Spherical convective dynamos in the rapidly rotating asymptotic regime. J Fluid Mech 813:558–593

Chapter 4

A catalogue of simulated jerks from a geodynamo model approaching Earth's core conditions

4DEarth_Swarm_Core ESA project deliverable D-E.1

J. Aubert
IPG Paris

4.1 General description

This document refers to publicly available output data from a geodynamo simulation that approaches closely to the physical conditions of Earth's core. In the model parameter space, this model is part of a series that defines a path connecting the conditions where classical dynamo models are found to those of the Earth's core. The theoretical definition of this path may be found in Aubert et al (2017), and the model described here is located at 71% of this path (path parameter $\epsilon = 10^{-5}$). This model is fully described in Aubert and Gillet (2021). Table 4.1 lists the key time scales and associated dimensionless numbers of this model together with those expected at Earth's core conditions.

From the dimensionless outputs of the numerical model, the provided data files are **already scaled to dimensional values**. Here I mention some details for the re-scaling procedure that has been applied. Re-scaling can be done in a completely self-consistent manner only once the model conditions reach those of the Earth's core. The path theory serves to rescale these quantities in a way that rationalizes the gap that still exists between those two conditions (Aubert, 2018, 2020). For the time series presented here, the time basis is provided by the choice of the magnetic diffusivity η in table 4.1. From there and the value of the magnetic Reynolds number Rm immediately follow the determination of the core overturn time τ_U involving the root-mean-squared flow velocity U in the shell and the re-scaling of the velocity field. The value of the Lundquist number gives access to the Alfvén time τ_A, which however differs from its target Earth value as we are not yet at the end of the path. The r.m.s dimensional magnetic field amplitude B can therefore be ob-

Quantity	Definition	71% of path model	Earth's core
Earth radius	a	6371.2 km	6371.2 km
core surface radius	r_o	3485 km	3485 km
outer core thickness	D	2260 km	2260 km
magnetic diffusivity	η	1.2 m^2/s	$\approx$ 1.2 m^2/s
magnetic diffusion time	$\tau_\eta = D^2/\eta$	135000 yr	$\approx$ 135000 yr
planetary rotation period	$2\pi\tau_\Omega = 2\pi/\Omega$	12 days	1 day
Alfvén time	$\tau_A = \sqrt{\rho\mu}D/B$	5.8 yr	$\approx$ 2 yr
1D Alfvén speed	$D/\sqrt{3}\tau_A$	225 km/yr	$\approx$ 650 km/yr
core overturn time	$\tau_U = D/U$	118 yr	$\approx$ 120 yr
1D convective speed	$D/\sqrt{3}\tau_U$	11 km/yr	$\approx$ 11 km/yr
Magnetic Ekman number	$E/Pm = \tau_\Omega/\tau_\eta$	3.8 10^{-8}	$\approx$ 3.2 10^{-9}
Magnetic Reynolds number	$Rm = \tau_\eta/\tau_U$	1140	$\approx$ 1100
Lundquist number	$S = \tau_\eta/\tau_A$	23300	$\approx$ 68000

Table 4.1: Key parameters for the model, presented together with their model values and values expected at Earth's core conditions. B and U are root-mean-squared amplitudes of the magnetic field inside the simulated core.

tained by considering that the density ρ of the simulated fluid shell is $(5.8/2)^2$ time stronger than its Earth counterpart $\rho = 11000\ \mathrm{kg/m^3}$, this former factor accounting for the differences in the model and Earth Alfvén times. Finally, the density anomaly field is rescaled following Aubert and Gillet (2021), by expressing the dimensionless field in units of $\rho\Omega\eta/g_oD$ (where g_o is the gravity at the core surface), and multiplying the result with Earth's core dimensional estimate for $\rho\Omega\eta/g_oD$ obtained with $g_o = 10\ \mathrm{m/s^2}$, $\rho = 11000\ \mathrm{kg/m^3}$ and the other values from Table 4.1.

Figure 4.1 presents temporal sequences of the core-mantle boundary secular acceleration energy (as defined in Aubert, 2018) and Earth-surface jerk energy (as defined in Aubert and Finlay, 2019). The outputs that are made available here specifically focus on the 14 simulated geomagnetic jerk events marked with arrows in Figure 4.1. These ouputs first consist in high-resolution time series of the coefficents describing the poloidal magnetic field outside the core and the velocity field at the core surface. The time series cover a few decades before and after the approximate timestamps of jerks presented in Table 4.2. Their temporal resolution is set to 0.05 years i.e. four times finer than the long time series covering the entire sequence that were previously provided in deliverable D-C.1. The model operates with stress-free boundary conditions, which implies that Ekman boundary layers are not described and that the core surface directly corresponds to the free stream. For each jerk event, a collection of movies representing these time series is also provided. Finally, full three-dimensional states of the simulation at selected times are provided for a selection of jerks.

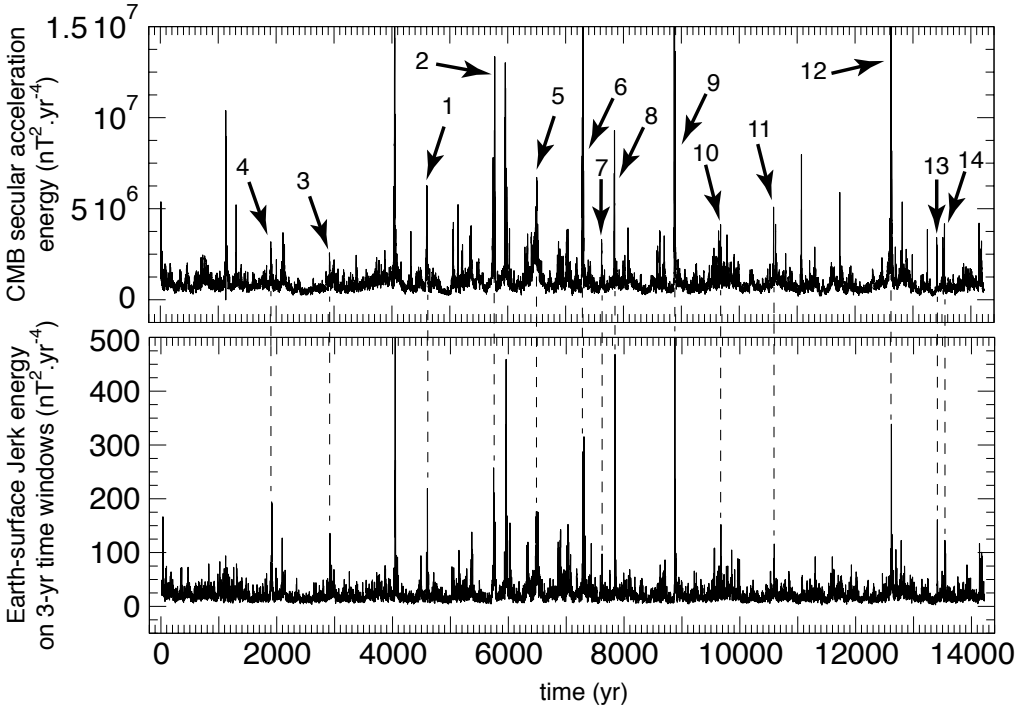

Figure 4.1: Core-mantle boundary (CMB) secular acceleration energy (top) and Earth-surface jerk energy (bottom), as functions of the dimensional simulation time. See Aubert (2018); Aubert and Finlay (2019) for definitions. Following these references, the outputs on this figure have been truncated at spherical harmonic degree and order 13, but the publicly available outputs are supplied up to a higher spherical harmonic resolution of 30.

Jerk No.	timestamp (years)	Jerk No.	timestamp (years)
1	4600	8	7840
2	5750	9	8880
3	2920	10	9673
4	1915	11	10590
5	6490	12	12620
6	7300	13	13411
7	7620	14	13546

Table 4.2: Approximate timestamps for simulated jerks in the catalog.

4.2 Data format and description

4.2.1 Magnetic field coefficients

To describe the magnetic field at and above the core surface, we adopt the classical Gauss coefficient description for the magnetic field. Denoting the colatitude as θ and the Greenwich-centered longitude as φ, the poloidal field at a radius r above the core-mantle boundary may be written

$$\mathbf{B}_{\boldsymbol{p}}(r,\theta,\varphi,t) = -\boldsymbol{\nabla} V \tag{4.1}$$

where

$$V(r,\theta,\varphi,t) = a\sum_{l=1}^{30}\left(\frac{a}{r}\right)^{l+1}\sum_{m=0}^{l}\left[g_l^m(t)\cos m\varphi + h_l^m(t)\sin m\varphi\right]P_l^m(\cos\theta). \tag{4.2}$$

Here t is time, $a = 6371.2$ km is Earth's magnetic radius of reference, P_l^m is the Schmidt-seminormalised Legendre function of degree l and order m.

For each jerk event, the file `Gauss_Bsurf.mat` (`MATLAB` data format) comprises the dimensional timestamp vector `timers` (in years) containing the discrete values of t and an array `gnm` containing the coefficients $g_l^m(t)$, $h_l^m(t)$ (in nanoteslas) arranged according to:

$$\begin{aligned}
\texttt{gnm}(:,1) &= g_1^0(t)\\
\texttt{gnm}(:,2) &= g_1^1(t)\\
\texttt{gnm}(:,3) &= h_1^1(t)\\
\texttt{gnm}(:,4) &= g_2^0(t)\\
\texttt{gnm}(:,5) &= g_2^1(t)\\
\texttt{gnm}(:,6) &= h_2^1(t)\\
\texttt{gnm}(:,7) &= g_2^2(t)\\
\texttt{gnm}(:,8) &= h_2^2(t)\\
&\ldots\\
\texttt{gnm}(:,959) &= g_{30}^{30}(t)\\
\texttt{gnm}(:,960) &= h_{30}^{30}(t)
\end{aligned}$$

Note that the sinus coefficients corresponding to $m = 0$ are not stored as they vanish identically. There are therefore 960 coefficients corresponding to a description of the output up to spherical harmonic degree and order 30. The core surface poloidal magnetic field is then obtained by setting r to $r_o = 3485$ km in equation (4.2).

4.2.2 Velocity field coefficients

The core surface velocity field coefficients are described using the spheroidal-toroidal formalism. The θ and φ components of the core surface velocity vector $\mathbf{u}$ are written

$$\mathbf{u} = \begin{pmatrix} u_\theta = \dfrac{1}{\sin\theta}\dfrac{\partial T}{\partial \varphi} + \dfrac{\partial S}{\partial \theta} \\ u_\varphi = -\dfrac{\partial T}{\partial \theta} + \dfrac{1}{\sin\theta}\dfrac{\partial S}{\partial \varphi} \end{pmatrix} \tag{4.3}$$

The spectral decomposition of T, S obeys

$$T = \sum_{l=1}^{30}\sum_{m=0}^{l}\left[tc_l^m(t)\cos m\varphi + ts_l^m(t)\sin m\varphi\right]P_l^m(\cos\theta) \tag{4.4}$$

$$S = \sum_{l=1}^{30}\sum_{m=0}^{l}\left[sc_l^m(t)\cos m\varphi + ss_l^m(t)\sin m\varphi\right]P_l^m(\cos\theta) \tag{4.5}$$

For each jerk event, the file `Gauss_Vsurf.mat` (`MATLAB` data format) contains the timestamp `timers` (in years) together with two arrays `tnm` and `snm` (in km.rad/yr) where the coefficients tc_l^m,ts_l^m and sc_l^m,ss_l^m are respectively stored. The ordering follows that of the magnetic field Gauss coefficients i.e.

$$\begin{aligned}
\texttt{tnm}(:,1) &= tc_1^0(t)\\
\texttt{tnm}(:,2) &= tc_1^1(t)\\
\texttt{tnm}(:,3) &= ts_1^1(t)\\
\texttt{tnm}(:,4) &= tc_2^0(t)\\
\texttt{tnm}(:,5) &= tc_2^1(t)\\
\texttt{tnm}(:,6) &= ts_2^1(t)\\
\texttt{tnm}(:,7) &= tc_2^2(t)\\
\texttt{tnm}(:,8) &= ts_2^2(t)\\
&\ldots\\
\texttt{tnm}(:,959) &= tc_{30}^{30}(t)\\
\texttt{tnm}(:,960) &= ts_{30}^{30}(t)
\end{aligned}$$

Note that the sinus coefficients corresponding to $m = 0$ are not stored as they vanish identically. As for the magnetic field coefficients above there are 960 coefficients for each scalar, corresponding to a description of the output up to spherical harmonic degree and order 30.

4.2.3 Movies

For each jerk event, a `.zip` archive is provided that contains the following `mp4` movie files:

- `Brcmb.mov` and `Brcmb13.mov`: core surface radial magnetic field (in mT), respectively at native (up to spherical harmonic degree 170) and truncated (up to spherical harmonic degree 13) resolutions,

- `Vpcmb.mov`: core surface azimuthal velocity field (in km/yr) at native resolution,
- `dVcmb.mov`: core surface azimuthal velocity acceleration (in km/yr^2) at native resolution,
- `SVcmb.mov`: core surface radial secular variation (first time derivative of the magnetic field, in μT/yr) up to spherical harmonic degree 13,
- `SAcmb.mov` and `SAsurf.mov`: core surface and Earth surface radial secular acceleration (second time derivative of the magnetic field, in nT/yr^2) up to spherical harmonic degree 13.

4.2.4 Full three-dimensional states

For jerks 1,3 and 9, two states of the simulations at native spatial resolution are provided as (very large) binary files `Gt1` and `Gt2`. The two states are closely spaced in time such that a time derivative can be reliably computed. The states can be loaded into computer memory by using the provided matlab script `parodyload_scaled.m`.

Once loaded, the following variables are present in `MATLAB` memory:

- the dimensional timestamp `timers` (in years),
- the numbers of grid points `nr=1248` in radius, `nt=256` in latitude and `np=512` in longitude, with longitude `np=1` referring to 180 degrees East in the Pacific.
- the vectors `r(1:nr)` of radii within the outer core (in km), `theta(1:nt)` of latitudes and `phi(1:np)` of longitudes (both in radians) defining the spherical coordinate frame,
- the three `(1:np,1:nt,1:nr)` arrays `Vr,Vt,Vp` of the outer core velocity field components (in km/yr),
- the three `(1:np,1:nt,1:nr)` arrays `Br,Bt,Bp` of the outer core magnetic field components (in mT),
- the `(1:np,1:nt,1:nr)` array `T` of the outer core scalar density anomaly field (in kg/m^3).

Bibliography

Aubert J (2018) Geomagnetic acceleration and rapid hydromagnetic wave dynamics in advanced numerical simulations of the geodynamo. Geophys J Int 214(1):531–547

Aubert J (2020) Recent geomagnetic variations and the force balance in Earth's core. Geophys J Int DOI 10.1093/gji/ggaa007, doi: 10.1093/gji/ggaa007

Aubert J, Finlay CC (2019) Geomagnetic jerks and rapid hydromagnetic waves focusing at Earth's core surface. Nature Geosci 12(5):393–398, DOI 10.1038/s41561-019-0355-1

Aubert J, Gillet N (2021) The interplay of fast waves and slow convection in geodynamo simulations nearing earth's core conditions. Geophys J Int DOI https://doi.org/10.1093/gji/ggab054

Aubert J, Gastine T, Fournier A (2017) Spherical convective dynamos in the rapidly rotating asymptotic regime. J Fluid Mech 813:558–593

Chapter 5

Re-analysis of magnetic data under spatio-temporal dynamo constraints

4DEarth_Swarm_Core ESA project deliverables D-D.1 and R-D.1

N. Gillet[1], M. Istas[1], T. Schwaiger[1]
[1] ISTerre Grenoble

5.1 Introduction

The core surface flow re-analyses presented below are based on the inversion scheme developed by Gillet et al (2019), namely an augmented state ensemble Kalman filter. This algorithm has been implemented into the `pygeodyn` software (Huder et al, 2019). The forward model is based on spatio-temporal cross-covariances (extracted from geodynamo data series) of the flow, the radial magnetic field, and the unresolved induction at the core surface. It consists of a multivariate auto-regressive model of order 1 (AR-1). At each epoch t, these quantities are described through vectors (respectively $\mathbf{u}(t)$, $\mathbf{b}(t)$ and $\mathbf{e}(t)$) that contain the spherical harmonic representation of the fields. The main modifications, in comparison to previously published re-analyses, are the following:

- We consider here a priori cross-covariances from the 71%-path dynamo (Aubert and Gillet, 2021, see D-C.1 data products), which improves the time-scale separation between the turn-over time and the Alfvén time in comparison of the 50%-path dynamo that was previously available (Aubert et al, 2017).
- The re-analysis step of the Kalman filter used into `pygeodyn` has been improved, in particular the estimation of the forecast covariance matrix for the magnetic field. This point, particularly important when re-analyzing GVO data, is addressed in section §5.2.
- We consider several sets of magnetic data that allow a reanalysis until 2020: Gauss coefficients data from the COV-OBS-x2 (Huder et al, 2020) and CHAOS-7 (Finlay et al, 2020) field models, and GVO data (Hammer et al, 2021) – see also the D-B.1 data products.

On the one hand, a preliminary analysis of the resulting core flow models is provided in section §5.4. It shows hints for propagating flow patterns at sub-decadal periods, which may be interpreted in the framework of QG Alfvén waves of of QG-MC modes. Flow models derived from geomagnetic field models are delivered at

`https://geodyn.univ-grenoble-alpes.fr/`

On the other hand, the reanalysis of GVO data lead us to face an unpredicted difficulty. There remains unmodelled signals that leak into the core field model. We suspect these are mainly from ionospheric origin (i.e. internal to the satellite orbits). Simple pre-processing (filtering) is apparently not enough to erase them. This point is illustrated in section §5.3, and we propose a strategy to face this difficulty. We highlight that this issue constitutes a timely research area, as interannual ionospheric field changes are not well documented or understood yet.

Both the inversion of Gauss coefficient field models and of GVO data call for a better handling of some unmodelled signals at interannual time-scales. More detailed analyses of these results will lead to collaborative publications involving colleagues from DTU and IPGP.

5.2 Improvements of the core flow inversion scheme

We use the notations $\overline{\mathbf{x}} = E[\mathbf{x}]$ for the statistical expectation and $\mathsf{P}_{xx} = E\left[\delta\mathbf{x}\delta\mathbf{x}^T\right]$ for the cross-covariance matrix, with $\delta\mathbf{x} = \mathbf{x} - \overline{\mathbf{x}}$.

In the `pygeodyn` software the analysis is performed in 2 steps, first on main field (MF) data to get the Gauss coefficients, then on secular variation (SV) data to get the augmented state (flow and errors of representativeness). So far for the first analysis we considered as the forecast covariance matrix $\mathsf{P}^f_{bb} = E\left[\delta\mathbf{b}^f\delta\mathbf{b}^{fT}\right]$ the cross-covariance matrix P^*_{bb} obtained from the entire series of available dynamo states (see Gillet et al, 2019). This behaves nicely when using Gauss coefficient data (Barrois et al, 2017), but we noticed that it allows a too large variability at the analysis step when using instead GVO data, inducing strong time changes in the analysed field $\mathbf{b}^a$ when the amount of observational constraints varies through time. This calls for improvements to be brought to the `pygeodyn` software.

We discretise the induction equation between two epochs using an Euler scheme:

$$\mathbf{b}_{t+\Delta t} = \mathbf{b}_t + \Delta t\left(\mathsf{A}_t\mathbf{u}_t + \mathbf{e}_t\right) , \tag{5.1}$$

where A_t depends on $\mathbf{b}_t$. If the flow is projected onto principle components (PC), it writes $\mathbf{u}_t = \mathbf{u}_0 + \mathsf{S}\mathbf{v}_t$, with $\mathbf{u}_0$ the background flow and $\mathbf{v}_t$ the PC representation of the flow. Then equation (5.1) becomes

$$\mathbf{b}_{t+\Delta t} = \mathbf{b}_t + \Delta t\left(\mathsf{A}_t\mathbf{u}_0 + \tilde{\mathsf{A}}_t\mathbf{v}_t + \mathbf{e}_t\right) , \tag{5.2}$$

with $\tilde{\mathsf{A}}_t = \mathsf{A}_t\mathsf{S}$. We consider N epochs between two analyses ($\Delta t_a = N\Delta t$), so that

$$\mathbf{b}_{t_a+\Delta t_a} = \mathbf{b}_{t_a} + \Delta t \sum_{i=1}^{N} \left(\mathsf{A}_{t_i}\mathbf{u}_0 + \tilde{\mathsf{A}}_{t_i}\mathbf{v}_{t_i} + \mathbf{e}_{t_i} \right) , \tag{5.3}$$

with $t_i = t_a + (i-1)\Delta t$. We look for $\mathsf{P}^f_{bb}(t_a + \Delta t_a) = E\left[\delta\mathbf{b}_{t_a+\Delta t_a}\delta\mathbf{b}^T_{t_a+\Delta t_a}\right]$. For the expectation term we make the approximation

$$\overline{\mathsf{A}_t\mathbf{u}_t} \simeq \mathsf{A}_t\overline{\mathbf{u}}_t = \mathsf{A}_t\mathbf{u}_0 + \tilde{\mathsf{A}}_t\overline{\mathbf{v}}_t \,, \tag{5.4}$$

i.e. most of the variability comes from the flow (in comparison with the magnetic field that is best constrained and varies less with time), so that

$$\overline{\mathbf{b}}_{t_a+\Delta t_a} = \overline{\mathbf{b}}_{t_a} + \Delta t \sum_{i=1}^{N} \left(\mathsf{A}_{t_i}\mathbf{u}_0 + \tilde{\mathsf{A}}_{t_i}\overline{\mathbf{v}}_{t_i} + \overline{\mathbf{e}}_{t_i} \right) , \tag{5.5}$$

and

$$\mathsf{P}^f_{bb}(t_a + \Delta t_a) = E\left[\left(\delta\mathbf{b}_{t_a} + \Delta t \sum_{i=1}^{N} \left(\tilde{\mathsf{A}}_{t_i}\delta\mathbf{v}_{t_i} + \delta\mathbf{e}_{t_i} \right) \right) \left(\delta\mathbf{b}_{t_a} + \Delta t \sum_{i=1}^{N} \left(\tilde{\mathsf{A}}_{t_i}\delta\mathbf{v}_{t_i} + \delta\mathbf{e}_{t_i} \right) \right)^T \right] . \tag{5.6}$$

Considering deviations in $\mathbf{b}_{t_a}$, $\mathbf{e}$ and $\mathbf{u}$ as independent we then obtain

$$\mathsf{P}^f_{bb}(t_a + \Delta t_a) = \mathsf{P}^a_{bb}(t_a) + \Delta t^2 \sum_{i=1}^{N}\sum_{j=1}^{N} \left(\tilde{\mathsf{A}}_{t_i} E\left[\delta\mathbf{v}_{t_i}\delta\mathbf{v}^T_{t_j}\right] \tilde{\mathsf{A}}^T_{t_j} + E\left[\delta\mathbf{e}_{t_i}\delta\mathbf{e}^T_{t_j}\right] \right) , \tag{5.7}$$

with $\mathsf{P}^a_{xx} = E\left[\delta\mathbf{x}^a_{t_a}\delta\mathbf{x}^{a\,T}_{t_a}\right]$ an analysis covariance matrix. On time increments short in front of the typical time-scales of the drift matrices for $\mathbf{v}$ and $\mathbf{e}$ (i.e. $\Delta t_a \ll 1/\lambda_{v,e}$, with $\lambda_{v,e}$ the eigen-values of the drift matrices), we have $\delta\mathbf{v}_{t_1} = \delta\mathbf{v}_{t_a}$ and

$$\text{for } i \geq 2,\ \delta\mathbf{v}_{t_i} \simeq \delta\mathbf{v}_{t_a} + \sqrt{\Delta t} \sum_{k=1}^{i-1} \mathbf{r}_{vk} \,. \tag{5.8}$$

$\mathbf{r}_v$ is the random forcing term that enters the AR-1 equation for $\mathbf{v}$ (i.e. most of the short term dispersion on the flow trajectories comes from the random walk term). A similar expression holds for $\delta\mathbf{e}_i$. Then

$$\begin{aligned} E\left[\delta\mathbf{v}_{t_1}\delta\mathbf{v}^T_{t_j}\right] &= \mathsf{P}^a_{vv}(t_a) \,, \\ \text{for both } i \text{ and } j \geq 2, \quad E\left[\delta\mathbf{v}_{t_i}\delta\mathbf{v}^T_{t_j}\right] &= \mathsf{P}^a_{vv}(t_a) + \Delta t \sum_{k=1}^{i-1}\sum_{k'=1}^{j-1} E\left[\mathbf{r}_{vk}\mathbf{r}_{vk'}\right] \,. \end{aligned} \tag{5.9}$$

Since $E\left[\mathbf{r}_{vk}\mathbf{r}_{vk'}\right] = \mathsf{P}_{rrv}\delta_{kk'}$, this last relation gives

$$\text{for both } i \text{ and } j \geq 2,\ E\left[\delta\mathbf{v}_{t_i}\delta\mathbf{v}^T_{t_j}\right] = \mathsf{P}^a_{vv}(t_a) + \Delta t \mathsf{P}_{rrv} \min(i-1, j-1) \,. \tag{5.10}$$

We now approximate A_t as being constant between two analyses (most of the time changes come from $\mathbf{v}$ and $\mathbf{e}$). Using the relation

$$\sum_{i=2}^{N}\sum_{j=2}^{N}\min(i-1,j-1) = \frac{N}{6} - \frac{N^2}{2} + \frac{N^3}{3}\,, \tag{5.11}$$

and $N\Delta t = \Delta t_a$, equation (5.7) then becomes

$$\begin{aligned}\mathsf{P}^f_{bb}(t_a+\Delta t_a) \simeq \quad & \mathsf{P}^a_{bb}(t_a) + \Delta t_a^2\left[\tilde{\mathsf{A}}_{t_a}\mathsf{P}^a_{vv}(t_a)\tilde{\mathsf{A}}^T_{t_a} + \mathsf{P}^a_{ee}(t_a)\right] \\ & + \frac{\Delta t_a^3}{3}\left(1 - \frac{3}{2N} + \frac{1}{2N^2}\right)\left[\tilde{\mathsf{A}}_{t_a}\mathsf{P}_{rrv}\tilde{\mathsf{A}}^T_{t_a} + \mathsf{P}_{rre}\right]. \end{aligned} \tag{5.12}$$

In a case with no uncertainty on the previous analysis state, the dispersion within the ensemble of $\mathbf{b}^f$ evolves $\propto \Delta t^{3/2}$ – from the last term in equation (5.12). Otherwise, if the dispersion in the fields $\mathbf{u}^a(t_a)$ and $\mathbf{e}^a(t_a)$ is important, the second term in (5.12) will dominate for short increments Δt_a, and the dispersion in $\mathbf{b}^f$ will evolve $\propto \Delta t$.

This new formulation has been introduced into `pygeodyn`, with some prerequisit:

- For calculating A_{t_a} in equation (5.12) we consider for the sake of simplicity $\mathsf{A}(\overline{\mathbf{b}}^a(t_a))$, where $\overline{\mathbf{b}}^a$ is the ensemble average of the MF analysis states – i.e. we consider that the MF does not evolves much between two analyses.

- To proceed with equation (5.12) at the 1st analysis step, the matrix P^a_{bb} must be initialized. A simple way would be to start with the dynamo prior P^*_{bb}, but this may generate large off-sets between the first analyses from the field model and from the GVO. The posterior covariance matrix P^a_{bb} after analysing a field model (warm-up) seems a more appealing choice. For the sake of simplicity, this P^a_{bb} is approximated as a diagonal matrix, with diagonal elements carrying the variance of the spread within the ensemble of $\mathbf{b}^a$ (from the warm-up) at the start time of the GVO re-analysis.

- As the ensemble size is not large enough to constrain well all off-diagonal terms of P^a_{bb}, we will consider only the diagonal elements of the empirically estimated P^a_{bb}. Similarly off-diagonal terms in P^a_{vv} and P^a_{ee} are considered as negligeable (which appears to be approximately true in practice).

- Equation (5.12) supposes that an analysis is performed every Δt_a. In some situations, the MF is not analysed at some analysis epochs (e.g. absence of GVO data between CHAMP and Swarm, or after Swarm, before CHAMP, etc.). We then replace in (5.12) Δt_a by $k\Delta t_a$, with k the number of analysis periods between two MF analyses.

An example of the effect of considering this new covariance matrix when considering GVO data is shown in Figure 5.2. In the next sections, the new implementation including equation (5.12) will be considered.

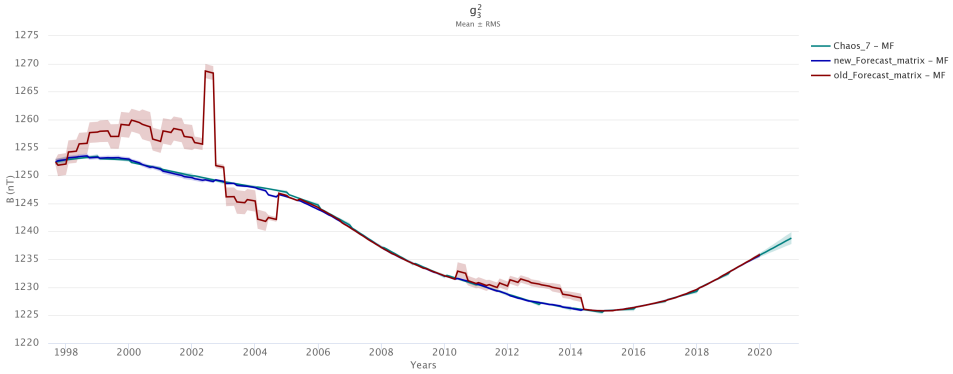

Figure 5.1: Impact of the use of the new derivation of P^f_{bb} on the Gauss coefficient g_3^2, for a re-analysis of GVO data from 1998 to 2020. In blue when using equation (5.12), in red with the ancient implementation (with the full dynamo covariances), and in Cyan with the CHAOS-7 model.

5.3 On the need for a more accurate processing of GVO data

Preliminary re-analyses using annual differences of 4-monthly means GVO as SV data show strong oscillations of the magnetic field field Gauss coefficients. We consider these are likely due to unmodelled ionospheric contributions, in particular because they mainly affect spherical harmonic orders $m = 0$ and $m = 1$ (see Figure 5.3, top). They subsequently imply spurious fluctuations in the core flow coefficients (Figure 5.3, middle). We do not know precisely down to which period observed field changes are mainly from internal origin.

As a first try to get around this difficulty, we built every 4 month sliding annual means from the 4-monthly GVO series. For all three components we then consider

$$\overline{Y}(t) = \frac{Y(t-1/2)}{6} + \frac{Y(t-1/6)}{3} + \frac{Y(t+1/6)}{3} + \frac{Y(t+1/2)}{6}\,, \tag{5.13}$$

where the time t is in years. This constitutes the filtered MF datasets, from which SV data are built every 4 months as centered differences of MF annual means:

$$\begin{aligned}\frac{d\overline{Y}}{dt}(t) &= \overline{Y}(t+1/3) - \overline{Y}(t-1/3) \\ &= \frac{Y(t+1/2) - Y(t-1/2)}{2} + \frac{Y(t+1/6) - Y(t-1/6)}{4} \\ &\quad + \frac{Y(t+5/6) - Y(t-5/6)}{4}\,.\end{aligned} \tag{5.14}$$

Our preliminary analysis using `pygeodyn` shows that if oscillations of periods shorter than 2 years (the Niquyst frequency with annual data) are indeed filtered

out, we see significant signals of period $\approx 3-4$ years that are not seen in CHAOS-7, and which induce large oscillations in core flow coefficients. These are unlikely realistic as they induce ways too large changes in the LOD (Figure 5.3, bottom).

We conclude for now that probably there remain unmodelled signals in the GVO datasets, internal to the satellites, which project onto the core field model. We favor a ionospheric source, as fields iunduced in the mantle are likely much weaker for realistic Q-responses (e.g. Olsen, 1999). This precludes for now the investigation of core flow changes from GVO on periods shorter than 3-4 years. This unforeseen effect calls for further investigations of these signals, which shall be carried out in collaboration with DTU. A first simple solution to this issue has been investigated: we mapped core surface flows without accounting for data at high latitudes (or only considering Z data). It however led to similar results. We highlight that there has been so far very few studies of interannual changes of the ionospheric field. These are neither well mapped nor understood.

The next step will consist of jointly inverting from GVO data the core field plus a source at an altitude representative of the ionosphere (see Ropp et al, 2020). Given the geometry of the target, for these extra model parameters we will design the prior covariance matrix so as to favor near-zonal coefficients (i.e. spherical harmonic orders $m = 0$ and $m = 1$). As there will necessarily be ambiguities between the two sources, we will start with a study of the sensitivity to the prior information added on the ionospheric field model. We are also currently implementing into `pygeodyn` the use of robust norms (instead of L2) for the measure of the misfit to GVO data (Farquharson and Oldenburg, 1998). This should help reduce the sensitivity of the internal field model to irregular external fields.

5.4 Core flow re-analyses from Gauss coefficient geomagnetic observations

The models illustrated below have been inverted from Gauss coefficient data of the COV-OBS.x2 and CHAOS-7 field models. In order to compare with an independent field model constructed upon an alternative method (the correlation-based approach, see Holschneider et al, 2016), we also use data from the MCM field model of Ropp et al (2020). The latter two inversion have been warmed-up using COV-OBS.x2 data prior to 1999.

The slowly varying flow models are very similar to previous estimates, showing the westward gyre largely documented over the past years (e.g. Pais and Jault, 2008; Gillet et al, 2009; Aubert, 2014; Gillet et al, 2019). We thus focus here on interannual flow changes, for which the extension of the satellite era to at least 2020 offers a better constraint. Based on the above observation on ambiguous field changes of 2-3 yr periods, we show below flow models band-pass filtered between 4 and 9.5 years, using a Butterworth filter of order 4. We remind that the temporal spectrum of core flows shows more power towards short period, so that there exists decadal changes with intensities larger than what is reported below.

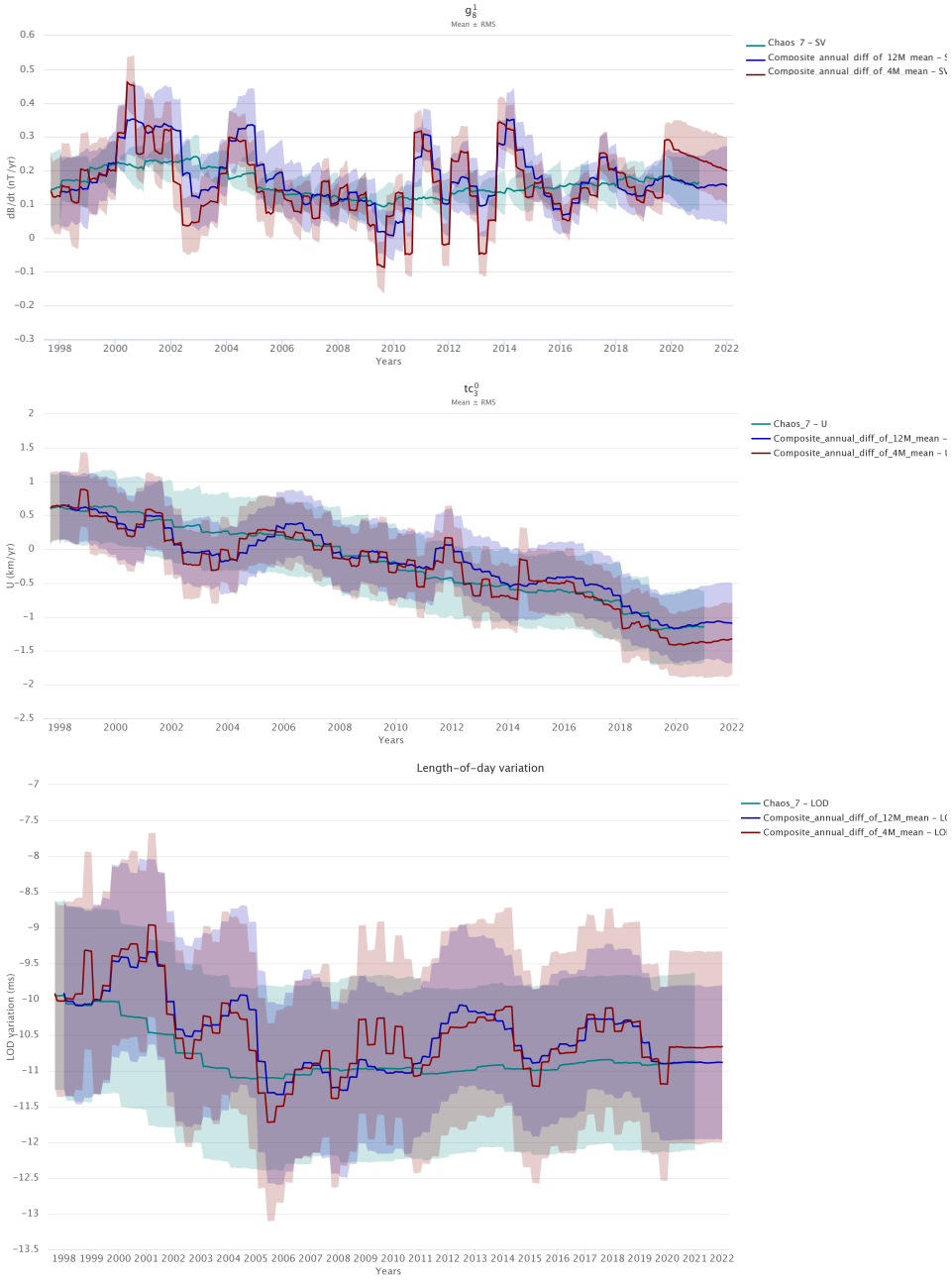

Figure 5.2: Re-analyses of the core-surface flow and magnetic field from 1998 to 2020, using several datasets: CHAOS-7 Gauss coefficients (cyan), 4-monthly GVO data (red) and annual means of 4-monthly GVO data (blue). top: SV coefficient g_8^1; middle: flow coefficient t_3^0; bottom: associated length-of-day (LOD) variations.

A preliminary analysis over the satellite era confirms some previous findings by Gillet et al (2019). In particular, focusing on sub-decadal flow changes, we see that the most intense dynamics takes place within the equatorial belt, with interannual velocities as large as 5 km/yr (Gillet et al, 2015; Finlay et al, 2016; Kloss and Finlay, 2019). Meanwhile, the accumulation of high quality satellite data through time allows a closer look at transient phenomena.

Our new models now covering over 20 yr of satellite data, we are able to more clearly isolate azimuthal flow patterns around the equator, with a periodicity of $\approx$ 7 yr. These features are seen from all three magnetic field models, with a reasonable coherence within the flow solutions – even though with MCM some more spatial compexity is observed, in particular in the Eastern hemisphere. The flow patterns seem to propagate Westward, starting from below the Greenwhich meridian to $\approx$ 150°E (see Figure 5.3). This would correspond to one circulation around the equator in about 14 yrs, i.e. a speed of $\sim$ 1500 km/yr at the core surface.

Meanwhile, the equatorial belt is the area of the core surface the better covered by magnetic data. Furthermore, it is less sensitive to the complex separation of magnetic sources at high latitudes. Indeed, the coherence between the three flow models seems less when looking away from the equator. We show in Figures 5.4 and 5.5 time-latitude diagrams of the band-pass filtered ortho-radial and azimuthal velocities for longitudes 180°E and 90°E. For all three models, these transient flows are predominantly equatorially symmetric. Away from the equator, motions are somewhat less intense when inverted from the CHAOS-7 model, in comparison with COV-OB-x2 and MCM. This may be related to the stronger damping applied on near zonal Gauss coefficients used when building the CHAOS-7 model. In some occurences, there is some hint of latitudinal propagation of flow patterns from several field models, as for instance towards the equator (resp. the poles) on u_θ (resp. u_ϕ) at 90°E (although we cannot exclude an artificial effect of the filtering). These signals reach the tangent cylinder from the core equator (and vice-versa) in about 5 years, corresponding to a speed of $\approx$ 800 km/yr at the core surface. We emphasize that interannual motions are not restricted to the Atlantic hemisphere; strong transient flows also show up in the Pacific hemisphere (see also Barrois et al, 2018).

The speeds and time-scales estimated above are commensurate with the Alfvén speed $V_A = B/\sqrt{\rho\mu}$, which spans 800 to 1400 km/yr for a magnetic field intensity $B \in [3, 5]$ mT. It is thus tempting to interprete the features documented here in the framework of QG Alfvén waves (Aubert and Finlay, 2019; Aubert and Gillet, 2021), and of propagating interannual QG-MC modes (Gerick et al, 2020). The former propagate mainly in the cylindrical radial direction in the path geodynamo simulations (although some Westward propagation has also been detected in some rare events, when the magnetic field configuration is appropriate for this). The latter propose a natural set of Wetsward propagating modes. However, if combined to one another in an out-of-phase manner, they may also give rise to propagation in the ortho-radial direction at the CMB.

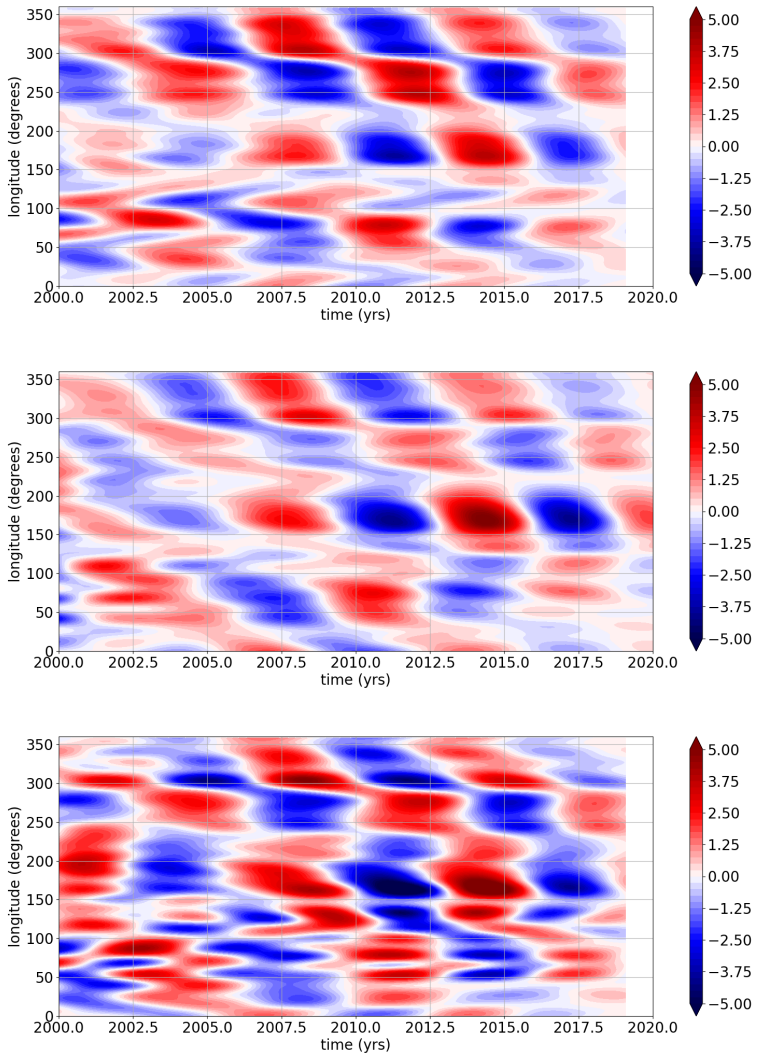

Figure 5.3: Time-longitude diagram of the azimuthal velocity (in km/yr) at the equator over 2000-2020, filtered at subdecadal periods, for the re-analysed core surface flow models over from Gauss coefficients of the MCM (bottom), CHAOS-7 (middle) and COV-OBS.x2 (top) field models.

Bibliography

Aubert J (2014) Earth's core internal dynamics 1840–2010 imaged by inverse geodynamo modelling. Geophys J Int 197(3):1321–1334

Aubert J, Finlay CC (2019) Geomagnetic jerks and rapid hydromagnetic waves focusing at Earth's core surface. Nature Geosci 12(5):393–398, DOI 10.1038/s41561-019-0355-1

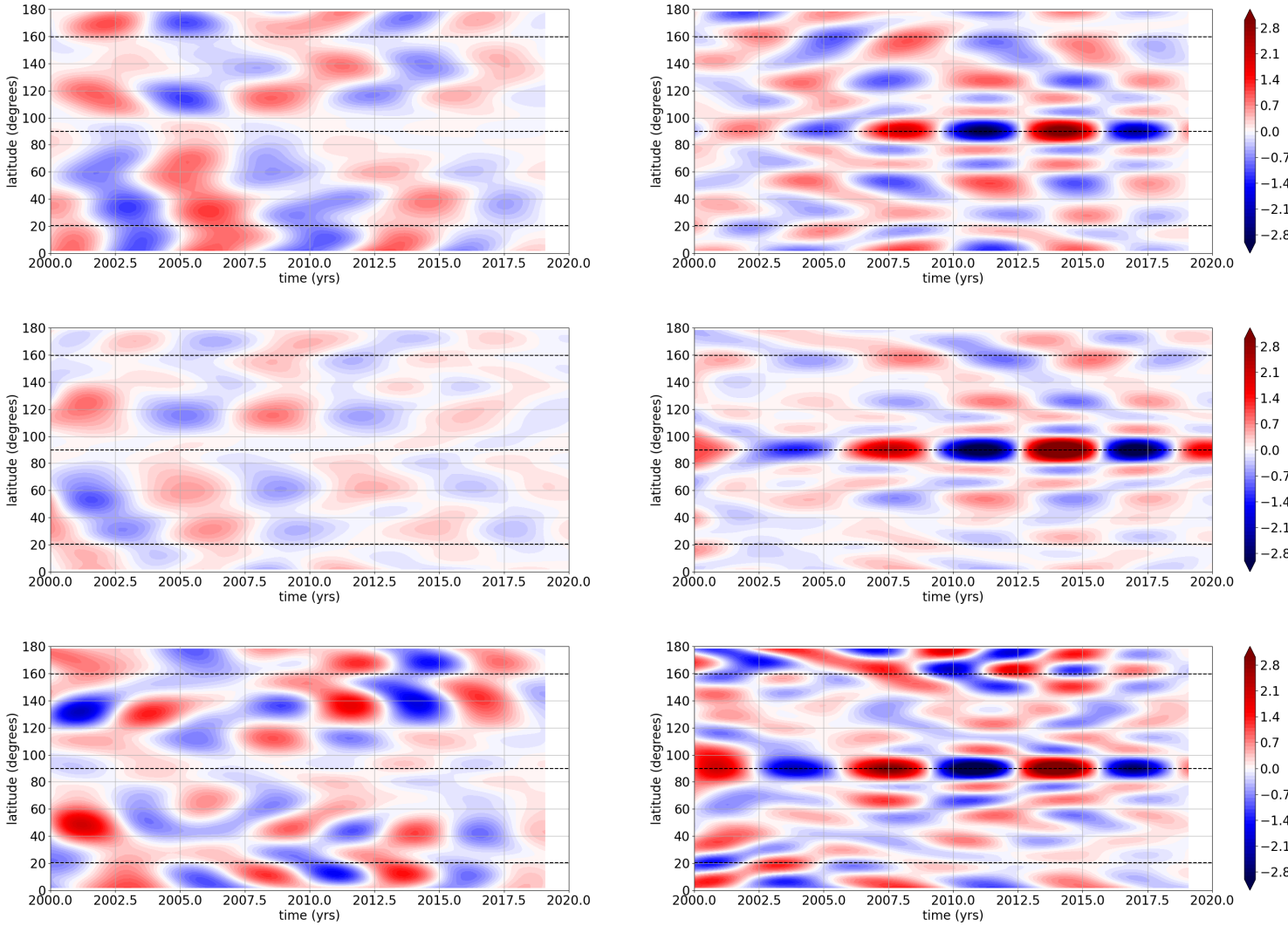

Figure 5.4: Time-latitude diagram of the orthoradial (left) and azimuthal (right) velocities (in km/yr) at 180°E over 2000-2020, filtered at subdecadal periods, for the re-analysed core surface flow models over from Gauss coefficients of the MCM (bottom), CHAOS-7 (middle) and COV-OBS.x2 (top) field models.

Aubert J, Gillet N (2021) The interplay of fast waves and slow convection in geodynamo simulations nearing earth's core conditions. Geophys J Int DOI https://doi.org/10.1093/gji/ggab054

Aubert J, Gastine T, Fournier A (2017) Spherical convective dynamos in the rapidly rotating asymptotic regime. J Fluid Mech 813:558–593

Barrois O, Gillet N, Aubert J (2017) Contributions to the geomagnetic secular vari-

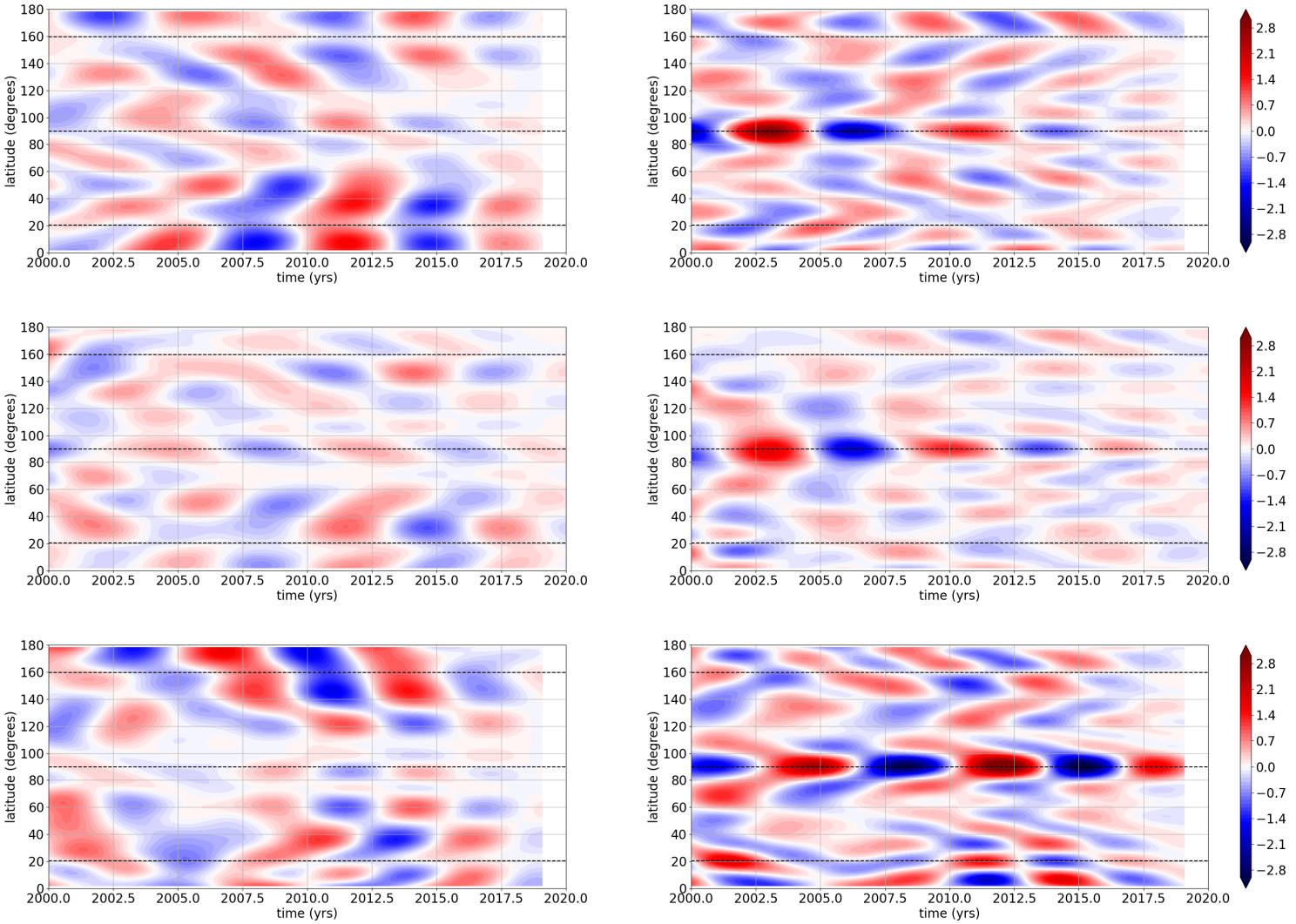

Figure 5.5: Time-latitude diagram of the orthoradial (left) and azimuthal (right) velocities (in km/yr) at 90°E over 2000-2020, filtered at subdecadal periods, for the re-analysed core surface flow models over from Gauss coefficients of the MCM (bottom), CHAOS-7 (middle) and COV-OBS.x2 (top) field models.

ation from a reanalysis of core surface dynamics. Geophys J Int 211(1):50–68

Barrois O, Hammer M, Finlay C, Martin Y, Gillet N (2018) Assimilation of ground and satellite magnetic measurements: inference of core surface magnetic and velocity field changes. Geophysical Journal International 215(1):695–712

Farquharson CG, Oldenburg DW (1998) Non-linear inversion using general mea-

sures of data misfit and model structure. Geophysical Journal International 134(1):213–227

Finlay CC, Olsen N, Kotsiaros S, Gillet N, Tøffner-Clausen L (2016) Recent geomagnetic secular variation from Swarm. Earth, Planets and Space 68(1):1–18

Finlay CC, Kloss C, Olsen N, Hammer MD, Tøffner-Clausen L, Grayver A, Kuvshinov A (2020) The chaos-7 geomagnetic field model and observed changes in the south atlantic anomaly. Earth, Planets and Space 72(1):1–31

Gerick F, Jault D, Noir J (2020) Fast quasi-geostrophic magneto-coriolis modes in the earth's core. Geophysical Research Letters p 2020GL090803

Gillet N, Pais M, Jault D (2009) Ensemble inversion of time-dependent core flow models. Geochemistry, Geophysics, Geosystems 10(6)

Gillet N, Jault D, Finlay C (2015) Planetary gyre, time-dependent eddies, torsional waves, and equatorial jets at the earth's core surface. Journal of Geophysical Research: Solid Earth 120(6):3991–4013

Gillet N, Huder L, Aubert J (2019) A reduced stochastic model of core surface dynamics based on geodynamo simulations. Geophys J Int 219(1):522–539

Hammer MD, Cox GA, Brown WJ, Beggan CD, Finlay CC (2021) Geomagnetic virtual observatories: monitoring geomagnetic secular variation with the swarm satellites. Earth, Planets and Space 73(1):1–22

Holschneider M, Lesur V, Mauerberger S, Baerenzung J (2016) Correlation-based modeling and separation of geomagnetic field components. J Geophys Res: Solid Earth 121(5):3142–3160

Huder L, Gillet N, Thollard F (2019) pygeodyn 1.1. 0: a python package for geomagnetic data assimilation. Geoscientific Model Development 12(8):3795–3803

Huder L, Gillet N, Finlay CC, Hammer MD, Tchoungui H (2020) Cov-obs.x2: 180 years of geomagnetic field evolution from ground-based and satellite observations. Earth, Planets and Space 72(1):1–18

Kloss C, Finlay CC (2019) Time-dependent low-latitude core flow and geomagnetic field acceleration pulses. Geophysical Journal International 217(1):140–168

Olsen N (1999) Induction studies with satellite data. Surveys in Geophysics 20(3):309–340

Pais M, Jault D (2008) Quasi-geostrophic flows responsible for the secular variation of the Earth's magnetic field. Geophys J Int 173(2):421–443

Ropp G, Lesur V, Baerenzung J, Holschneider M (2020) Sequential modelling of the earth's core magnetic field. Earth, Planets and Space 72(1):1–15

Chapter 6

QG-MAC inversion scheme from 3D simulations

4DEarth_Swarm_Core ESA project deliverable R-C.1

J. Aubert
IPG Paris

This deliverable is contained in the following publication: J. Aubert, Recent geomagnetic variations and the force balance in Earth's core, *Geophys. J. Int.*, 221(1), 2020, 378–393, https://doi.org/10.1093/gji/ggaa007

abstract:

The nature of the force balance that governs the geodynamo is debated. Recent theoretical analyses and numerical simulations support a quasigeotrophic (QG), magneto-Archimedes-Coriolis (MAC) balance in Earth's core, where the Coriolis and pressure forces equilibrate at leading order in amplitude, and where the buoyancy, Lorentz and ageostrophic Coriolis forces equilibrate at the next order. In contrast, earlier theoretical expectations have favoured a magnetostrophic regime where the Lorentz force would reach leading order at the system scale. The dominant driver (buoyant or magnetic) for the general circulation in Earth's core is equally debated. In this study, these questions are explored in the light of the high-quality geomagnetic data recently acquired by satellites and at magnetic ground observatories. The analysis involves inverse geodynamo modelling, a method that uses multivariate statistics extracted from a numerical geodynamo model to infer the state of Earth's core from a geomagnetic field model interpretation of the main field and secular variation data. To test the QG-MAC dynamic hypothesis against the data, the framework is extended in order to explicitly prescribe this force balance into the inverse problem solved at the core surface. The resulting inverse solutions achieve a quantitatively adequate fit to the data while ensuring deviations from the QG-MAC balance (which amount to an inertial driving of the flow) lower than each of the leading forces. The general circulation imaged within the core over the past two decades confirms the existence of a planetary-scale, eccentric, axially columnar gyre that comprises an intense, equatorially symmetric jet at high latitudes in the Pacific hemisphere. The dominant driver of this circulation is

shown to be of buoyant nature, through a thermal wind balance with a longitudinally hemispheric buoyancy anomaly distribution. Geomagnetic forecasts initiated with the inverted core states are systematically more accurate against the true interannual geomagnetic field evolution when enforcing the QG-MAC constraint. This force balance is therefore consistent with the geomagnetic data at the large scales of Earth's core that can be imaged by the method.

Chapter 7

The QG model using the Lagrangian formalism

4DEarth_Swarm_Core ESA project deliverable R-F.1

F. Gerick[1], D. Jault[1] and J. Noir[2]
[1]ISTerre Grenoble, [2]ETH Zurich

This deliverable is contained in the following publication: F. Gerick, D. Jault, J. Noir and J. Vidal, Pressure torque of torsional Alfvén modes acting on an ellipsoidal mantle, *Geophys. J. Int.*, 222(1), 2020, 338–351, https://doi.org/10.1093/gji/ggaa166

abstract:

We investigate the pressure torque between the fluid core and the solid mantle arising from magnetohydrodynamic modes in a rapidly rotating planetary core. A 2-D reduced model of the core fluid dynamics is developed to account for the non-spherical core–mantle boundary. The simplification of such a quasi-geostrophic model rests on the assumption of invariance of the equatorial components of the fluid velocity along the rotation axis. We use this model to investigate and quantify the axial torques of linear modes, focusing on the torsional Alfvén modes (TM) in an ellipsoid. We verify that the periods of these modes do not depend on the rotation frequency. Furthermore, they possess angular momentum resulting in a net pressure torque acting on the mantle. This torque scales linearly with the equatorial ellipticity. We estimate that for the TM calculated here topographic coupling to the mantle is too weak to account for the variations in the Earth's length-of-day.